Stem Cell Reports
Article

ISSCR

OPEN ACCESS

Electrophysiological Maturation of Cerebral Organoids Correlates with Dynamic Morphological and Cellular Development

Summer R. Fair,[1,9] Dominic Julian,[1,9] Annalisa M. Hartlaub,[2] Sai Teja Pusuluri,[2] Girik Malik,[2,6] Taryn L. Summerfied,[2] Guomao Zhao,[8] Arelis B. Hester,[1] William E. Ackerman IV,[8] Ethan W. Hollingsworth,[1] Mehboob Ali,[2] Craig A. McElroy,[3] Irina A. Buhimschi,[8] Jaime Imitola,[7] Nathalie L. Maitre,[2] Tracy A. Bedrosian,[1] and Mark E. Hester[1,4,5,*]

[1]The Steve and Cindy Rasmussen Institute for Genomic Medicine, Abigail Wexner Research Institute at Nationwide Children's Hospital, 575 Children's Crossroad, Columbus, OH 43205-2716, USA
[2]Center for Perinatal Research, Abigail Wexner Research Institute at Nationwide Children's Hospital, Columbus, OH, USA
[3]College of Pharmacy, The Ohio State University Wexner Medical Center, Columbus, OH, USA
[4]Department of Pediatrics, The Ohio State University Wexner Medical Center, Columbus, OH, USA
[5]Department of Neuroscience, The Ohio State University Wexner Medical Center, Columbus, OH, USA
[6]Khoury College of Computer Sciences, Northeastern University, Boston, MA 02115, USA
[7]Department of Neurology, Laboratory for Neural Stem Cells and Functional Neurogenetics, University of Connecticut School of Medicine, Farmington, CT, USA
[8]Department of Obstetrics and Gynecology, University of Illinois at Chicago College of Medicine, Chicago, IL 60612, USA
[9]These authors contributed equally
*Correspondence: mark.hester@nationwidechildrens.org
https://doi.org/10.1016/j.stemcr.2020.08.017

SUMMARY

Cerebral organoids (COs) are rapidly accelerating the rate of translational neuroscience based on their potential to model complex features of the developing human brain. Several studies have examined the electrophysiological and neural network features of COs; however, no study has comprehensively investigated the developmental trajectory of electrophysiological properties in whole-brain COs and correlated these properties with developmentally linked morphological and cellular features. Here, we profiled the neuroelectrical activities of COs over the span of 5 months with a multi-electrode array platform and observed the emergence and maturation of several electrophysiologic properties, including rapid firing rates and network bursting events. To complement these analyses, we characterized the complex molecular and cellular development that gives rise to these mature neuroelectrical properties with immunohistochemical and single-cell transcriptomic analyses. This integrated approach highlights the value of COs as an emerging model system of human brain development and neurological disease.

INTRODUCTION

Our understanding of mammalian brain development has largely been derived from rodent models. Although these models have provided invaluable mechanistic insight, they are significantly limited in that they do not fully recapitulate the molecular, structural, and genetic complexity of human conditions. For example, human brains exemplify unique anatomical features, such as an expanded outer subventricular zone (SVZ), that are not present in mice (Sousa et al., 2017). This zone contains basal radial glia (bRG) that are critical for human cortical expansion (Fietz et al., 2010; Hansen et al., 2010; Johnson et al., 2015). Furthermore, our current knowledge of human brain development is largely based on analyses of postmortem or pathological specimens. Although they have provided important fundamental knowledge, these tools are not amenable to experimental manipulation (Hartlaub et al., 2019; Stiles and Jernigan, 2010).

Recent advances in stem cell and three-dimensional tissue culture techniques led to the advent of cerebral organoids (COs) that can model early periods of human fetal brain development (Camp et al., 2015; Hester and Hood, 2017; Lancaster et al., 2013; Lancaster and Knoblich, 2014; Qian et al., 2016; Quadrato et al., 2017; Yin et al., 2016). COs, which are generated from human pluripotent stem cells, are three-dimensional structures that can self-organize to form discrete regions of the human brain, such as the cerebral cortex. Several CO protocols have been developed that rely either on intrinsic patterning molecules or on exposure to morphogens under directed differentiation. Protocols that rely on spontaneous cues generate COs with diverse cell populations and multiple regional brain identities at the expense of increased interorganoid variability compared with directed differentiation approaches (Pasca, 2018).

Despite significant advances in discerning the morphological and cellular complexity of COs, very little work has been done to characterize their electrophysiological (EP) properties. A previous report showed the presence of spontaneous activity arising from photosensitive, retinal-like cells using a 64-channel neural probe implanted within 8-month-old whole-brain COs (Quadrato et al., 2017). Other studies performed EP measurements on organoid slices using whole-cell patch-clamp techniques (Birey et al., 2017;

Xiang et al., 2017) or measured network activity in COs via imaging of synchronized calcium activities (Sakaguchi et al., 2019). Most recently, Trujillo et al. used a forebrain organoid model to compare organoid EP features to EEG signatures from premature infants (Trujillo et al., 2019).

Here we examine the EP development of COs using a 64-channel multi-electrode array (MEA) array platform. This culture method enabled us to detect weak spontaneous electrical activity in COs after as early as 1 month in culture. We noted the gradual evolution of EP features in COs within 3 months in culture, as evidenced by elevated mean spike rates and characteristic spontaneous action potentials with discrete depolarizations. In addition, we characterized the simultaneous development of morphological and transcriptomic features in COs with immunohistochemistry (IHC) and single-cell RNA sequencing (scRNA-seq). Maturation of electrical features correlated with dynamic changes in the development of cell types within COs, such as the emergence of astrocytes and diverse neuronal populations. Last, as COs transition into increased cellular and morphological complexity, we observed activation of the neurotrophin (NTR)/TRK receptor signaling pathway. Our findings highlight the use of COs as a model not only for recapitulating complex morphological features of human brain development, but also as a functional testing platform to investigate how genetic and environmental factors perturb the development and maturation of neural circuits. Further, our results provide an impetus to use COs as a system to screen and functionally characterize potential pharmaceutical neuromodulators and gene therapeutics that would restore proper EP function in neurodevelopmental disorders.

RESULTS

Generation of COs from Human Induced Pluripotent Stem Cells

To investigate the contribution of diverse human brain cell types to the developmental maturation of electrical properties in COs, we used an undirected differentiation approach to generate human whole-brain COs (Di Lullo and Kriegstein, 2017; Hester and Hood, 2017; Lancaster et al., 2013; Pasca, 2018). Specifically, we used our previously described methods to generate human whole-brain COs based on a modified protocol from Lancaster et al. (Hester and Hood, 2017; Lancaster et al., 2013) (Figure 1A). We incorporated BrainPhys medium in our methodology, which has been shown to enhance neuronal synaptic function and promote the EP maturation of neuronal monolayer cultures (Bardy et al., 2015) and has not been previously used for long-term culture of COs (Figure 1A). We generated COs from a well-characterized human induced pluripotent stem cell (hiPSC) line (Burridge et al., 2011) that exhibits molecular characteristics of pluripotency (Figures S1A–S1E). These COs showed similar growth properties compared with previously established protocols (Figure 1B). Of note, the hiPSC-derived neuroepithelial (NE) bodies that give rise to the COs had translucent borders (Figure 1C) and expanded into NE buds at day 17 in culture (Figure 1D), similar to the developmental timing seen in conventional culture methods (Figures S1F–S1H). When switched to constant agitation culture conditions, COs showed steady growth characteristics (Figures 1B, 1E, and 1F) and did not significantly increase in growth area after day 60 in culture. Molecular analyses of early-stage CO cultures at day 25 revealed abundant proliferative $SOX2^{+}$ neural progenitor cells (NPCs) organized into neuroepithelium-like structures as shown by the expression of the cell-cycle marker Ki67 and the mitosis-specific cell-cycle marker pHH3 (Figures S1I and S1J).

Probing Electrical Activities in COs Using an MEA Platform

To probe the electrical activities of maturing whole-brain COs, we established a method to monitor their spontaneous electrical activity with a 64-channel MEA platform to detect and record extracellular field potential change activity (Figures 1G–1K). Planar MEA systems have a non-invasive, multi-site, electrical recording interface to functionally assay the electrophysiology of neuronal cultures. MEAs have been widely used with monolayer neuronal cultures to study their neurophysiology (Kizner et al., 2019; Mehta et al., 2018), although the application of MEAs to the study of EP features in three-dimensional whole-brain COs is underexplored. Since CO cultures require agitation in suspension to enhance nutrient diffusion and maintain optimal three-dimensional growth conditions, we developed a non-destructive method to functionally assay their surface electrical activities (Figures 1G–1K). Specifically, in this method, COs are transferred onto an MEA probe to record spontaneous electric activities. This protocol allowed us to identify the precise developmental timing of EP property emergence in COs. Since the recording distances of MEAs are not expected to be greater than 60 μm (Delgado Ruz and Schultz, 2014), we expected to measure electrical activities not only from superficial layer neurons positioned up to three cell layers from the surface layer Cajal-Retzius (CR) cells. In addition, based on the developmental time points at which we performed the MEA analyses, we expected to record from a diverse set of excitatory and inhibitory neuronal populations.

Evolution of EP Properties in COs

Using a 64-channel MEA array, we investigated the earliest time point at which electrical activity emerges in COs. We

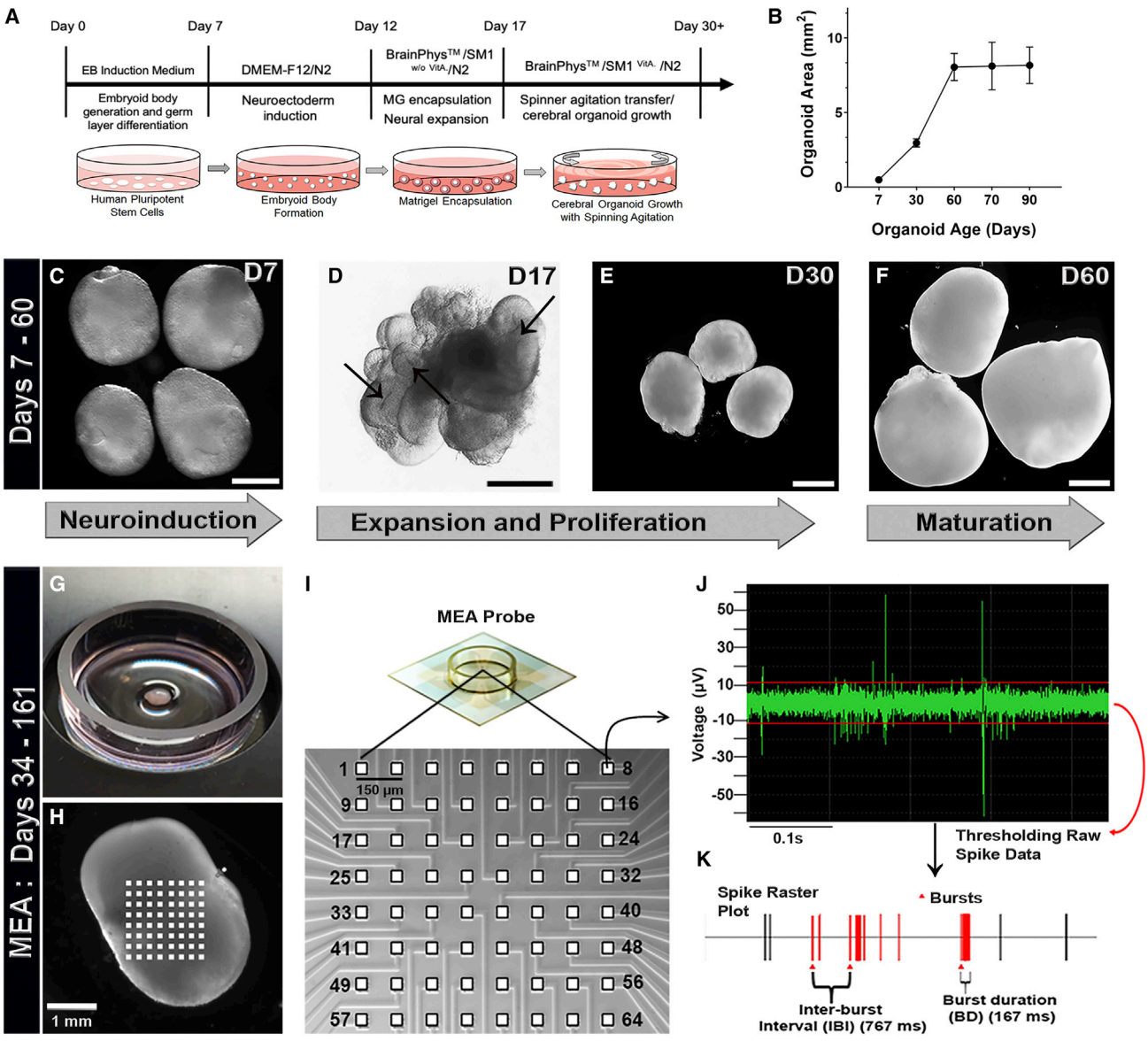

Figure 1. CO Protocol Timeline and Early-Stage Morphological Features

(A) Timeline of major developmental features and technical milestones in generating human COs. EB, embryoid body; MG, Matrigel encapsulation; VitA, vitamin A.

(B) Growth curve of organoid areas shows a plateau at day 60 (minimum of four independent organoids per time point). Data are presented as mean ± SEM.

(C) Encapsulated NE body that has been induced toward neuroectoderm. Scale bar, 200 µm.

(D) Encapsulated NE body with expanding neuroepithelial folds (black arrows). Scale bar, 100 µm.

(E) Day 30 COs. Scale bar, 1 mm.

(F) Day 60 COs. Scale bar, 1 mm.

(G and H) Spontaneous electrical activity can be detected from COs using a multi-electrode array (MEA) system. (G) A transferred CO on an MEA probe during acquisition of spontaneous electrical activity. (H) CO recording setup with 64 planar microelectrodes.

(I) Microelectrode array at high magnification.

(J) Local field potential trace from an individual microelectrode.

(K) Spike raster plot depicting electrical activities derived from a CO. Bursts are represented as red triangles.

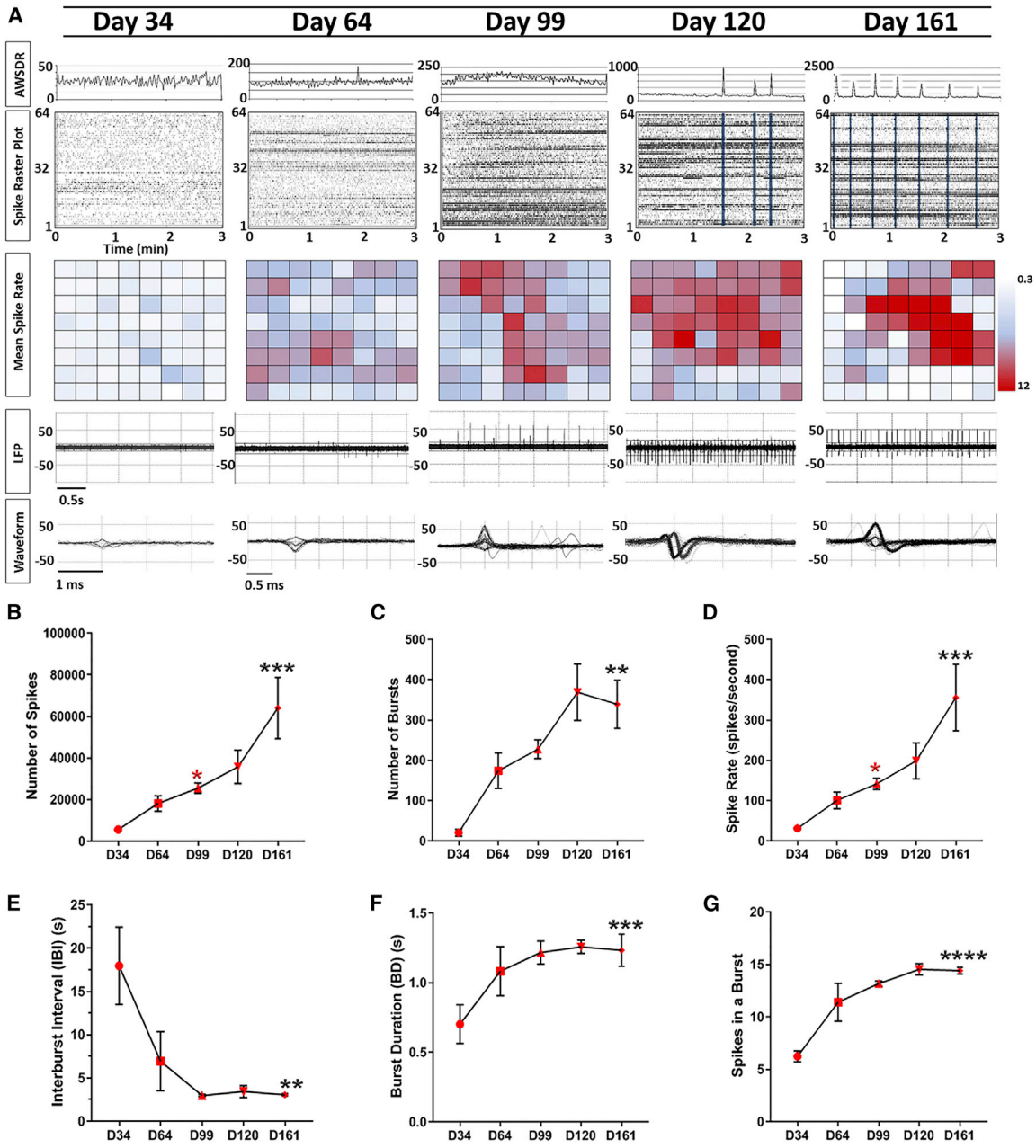

Figure 2. Developmental Trajectories of Electrophysiological Properties in COs

(A) Detection of spontaneous electrical activity in day-34 COs and approximately every month thereafter shows a progressive increase in and complexity of EP properties. Top: Graphical representation of the array-wide spike detection rate (AWSDR) above every spike raster plot with a 3-min recording interval. Synchronized burst firing (SBF) activity is observed in late-stage CO cultures and is indicated by light blue columns within raster plots of days 120 and 161. Note the corresponding peaks in the AWSDR above each SBF. Middle: Heatmap plots of the mean spike rates of neurons within COs recorded by each individual microelectrode. Bottom: Local field potential (LFP) traces and a corresponding waveform taken from a shorter time interval showing a progressive increase in voltage amplitude and spiking rate at successive developmental time points. Note the characteristic action potential waveforms shown in days 99, 120, and 161.

(B–G) EP quantifications of developing COs at approximately monthly intervals initiating at day 34 (n = 4/time point). EP data include (B) number of spikes, (C) number of bursts, (D) spike rate (number of spikes/s), (E) interburst interval, (F) burst duration, and (G) number of spikes in a burst. Data are presented as mean ± SEM and statistical analyses were performed using one-way ANOVA with Tukey's multiple

(legend continued on next page)

detected weak spiking activity (Figure 2) at day 34 in culture, which is expected, as this time point is correlated to a developmental window of rapid expansion of neuroepithelium and the beginning of early neurogenesis within COs that precedes neuronal maturation (Figures 1D, S1I, and S1J). After day 64 in culture, COs exhibited increases in both mean spike rate and field spike amplitude (local field potential), with both properties continuing to increase thereafter into day 99 of culture (Figures 2A and 2D). In addition, cortical neurons in COs showed characteristic spontaneous action potentials with discrete depolarizations (waveforms in days 120 and 161) that coincided with the observed expansion of astrocytes (Figures 4F, 4G, and 2A). At day 120, as indicated by a significant increase in the array-wide spike detection rate, COs exhibited synchronized burst firings (SBFs), which are prominent characteristic features of functional cortical neural networks in the developing mammalian cortex and a hallmark of synaptic signal propagation (Figure 2A). Day 161 COs showed further increases in the number of SBFs, which suggests the COs formed highly interconnected neural networks (Figure 2). Network burst metrics were analyzed in day 161 COs and showed an average network burst duration of 985 ± 152 ms, an average spike number of 1700 ± 300 in a network burst, and an average network burst interval of 25.3 ± 4.2 s. We observed a significant increase in the number of spikes, bursts, and spike rates over time in culture, which reflects the neuronal synaptic maturation of electrical transmission within COs (Figures 2B–2G). Altogether, these results demonstrate that COs show a gradual evolution of EP properties over development that resembles hallmark features of the developing neonatal brain. This trajectory begins in day 30–64 culture when COs have immature electrical activities as evidenced by random, low-amplitude, spike events and matures as more complex network bursting events or SBFs emerge by day 120 and increase to day 161.

Increased Cellular Diversity in COs and Correlation with Their Electrophysiological Trajectories

To correlate the trajectories of electrical activities we observed in COs to their morphological and molecular properties, we performed scRNA-seq in COs and IHC analyses of neuronal and glial lineages. We first subjected COs to scRNA-seq at late developmental time points, including days 93 and 140, to characterize the dynamic transcriptome of their diverse cell types (Figures 3 and S2A). We performed unsupervised clustering on gene expression profiles from an integrated dataset of 8,578 cells (Figures 3A and 3B) and identified eight major clusters using known cell-type-specific marker genes (Figures 3C and S2A). Excitatory cortical neurons (*NEUROD4*$^+$) and inhibitory interneurons (*GAD2*$^+$ and *DLX5*$^+$) comprised approximately 50% and 2% of all cells in day 93 COs, respectively, and approximately 24% and 30% of all cells in day 140 COs, respectively. The presence of inhibitory neurons in late-stage COs may indicate the maturation of local cortical circuitry within neuronal networks, which correlates with the maturation of EP properties we observed, such as the high degree of SBFs observed in day 161 COs (Figure 2). This developmental link supports their previously described role in the establishment and control of neural network activity (Kuijlaars et al., 2016; Mann and Paulsen, 2007). We also identified several non-neuronal populations, including proliferative progenitors (*MKI67*$^+$, *NUSAP1*$^+$), glia (*GFAP*$^+$, *HOPX*$^+$), and intermediate progenitors (*EOMES*$^+$, *NHLH1*$^+$), that had approximately equal representation in both day 93 and day 140 COs. The role of glia and progenitor populations in neurogenesis, neuronal maturation, and neural network activity has been extensively characterized in the developing human brain (Felix et al., 2020; Wilton et al., 2019). Their stable presence in early- and late-stage COs is likely a reflection of their similar functions in developing COs.

To complement our scRNA-seq analyses, we also performed a comprehensive IHC analysis of key cell-type-specific markers during CO development. At day 40, COs showed expansion of neuroepithelium as revealed by expression of the telencephalic markers FOXG1 and LHX2 (Figure S2B). *LHX2* displayed a more restrictive expression pattern in day 40 COs compared with *FOXG1* expression, coinciding with its predominate expression in the dorsal telencephalon (Godbole et al., 2018). *LHX2* maintained expression at day 93 in proliferative progenitors and a subset of excitatory neurons, although expression diminished at day 140 (Figure S2C). In contrast, *FOXG1* maintained robust expression in both excitatory and inhibitory neurons at days 93 and 140 (Figure S2C). In addition, the mitotic NPC marker SOX2 was expressed in the proliferative neuroepithelium at day 40 (Figure S2B) and absent in postmitotic neurons, as expected (Figure S2C). Further, IHC analysis of SOX2 at day 60 revealed expression in NPCs, which lined ventricle-like structures within COs and also expanded minimally in SVZ-like zones (Figure 4A). Similarly, PAX6, a dorsal cortical marker, which is characteristically expressed in radial glial (RG) cells, was also expressed predominately at ventricular zone (VZ)-like zones (Figure 4B). We also performed a more extensive

comparisons test (n = 4 independent organoids per time point recorded and 2 independent experiments performed). Differences between day 34 and day 161 or between day 99 and day 161 time points are shown by black or red asterisks, respectively. *p ≤ 0.05; **p ≤ 0.01; ***p ≤ 0.001; ****p ≤ 0.0001. All statistical analyses are shown in Table S3.

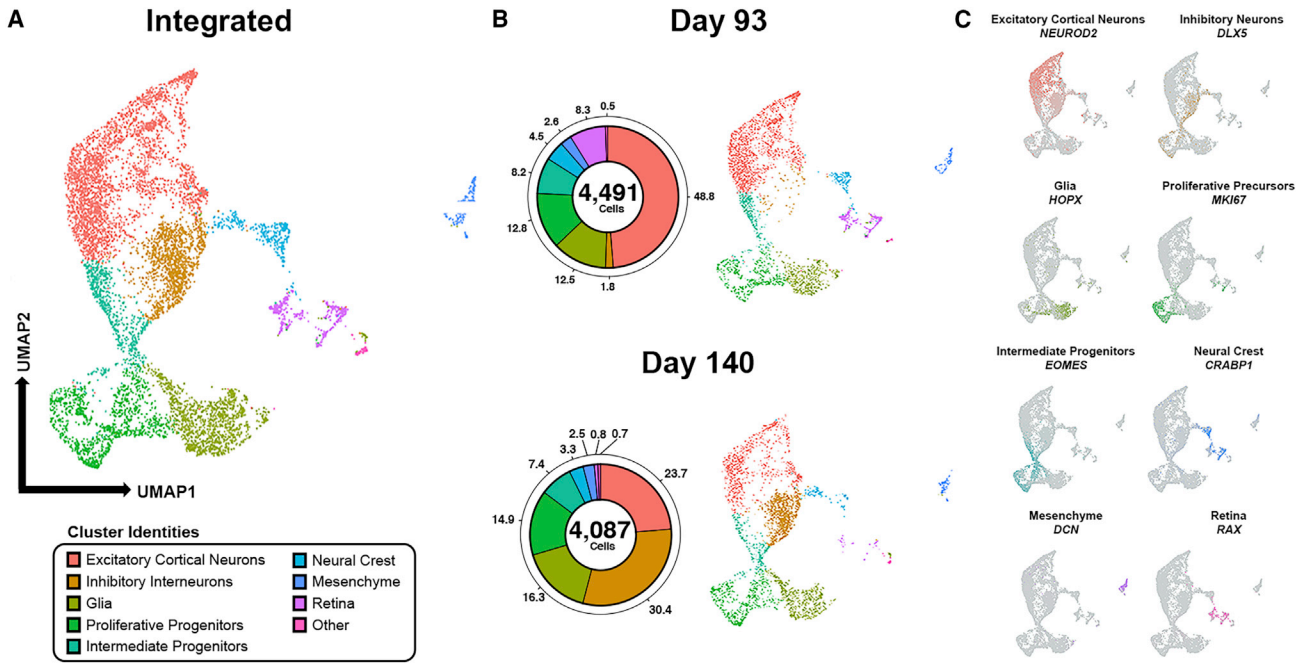

Figure 3. scRNA-seq Reveals Dynamic Cell Type Diversity Throughout the Developmental Trajectory of COs

(A) Uniform-manifold approximation map (UMAP) of single-cell RNA-sequencing data from two COs with 8,578 cells total analyzed in one independent experiment. Each point on the UMAP represents a single cell. Color map specifies cell type, as outlined in the legend.

(B) Donut plots and UMAPs for day 93 and day 140 capture of the cell type diversity within COs as a function of time. Day 93: 4,491 cells shown, including 2,190 excitatory cortical neurons (48.8%), 79 inhibitory interneurons (1.8%), 560 glia (12.5%), 575 proliferative progenitors (12.8%), 370 intermediate progenitors (8.2%), 203 neural crest (4.5%), 116 mesenchyme (2.6%), 373 retina (8.3%), and 25 other (0.5%). Day 140: 4,087 cells shown, including 968 excitatory cortical neurons (23.7%), 1,242 inhibitory interneurons (30.4%), 667 glia (16.3%), 608 proliferative progenitors (14.9%), 304 intermediate progenitors (7.4%), 133 neural crest (3.3%), 104 mesenchyme (2.6%), 34 retina (0.8%), and 27 other (0.7%).

(C) UMAPs depict canonical markers for each cell cluster type, *excluding other*. Additional markers are provided in Figure S4.

analysis of markers for neuronal subtypes within progenitor zone-like and cortical plate (CP)-like regions at day 60. As shown in Figure S3B, CTIP2$^+$ and TBR1$^+$ neurons are observed extensively within CP-like regions, and TBR2$^+$ neurons are restricted predominately to the SVZ-like zones. We also observed SOX2$^+$/HOPX$^+$ progenitors within VZ-like zones and the cortical layer 1 marker, REELIN, expressed at the most upper cortical layer that contains CR cells (Figure S3B). We and others also observe transient survival of CR neurons in COs (Renner et al., 2017), as indicated by low levels of *RELN* expression in day 140 COs (Figure S5A).

We further investigated the cellular composition of day 60 COs and observed a minor population of astrocytes emerging, as shown by GFAP expression (Figures 4C and 4D), that expanded significantly after an additional 26 days in day 86 COs (Figures 4F, 4G, and S3A). We found that our transcriptomic data were in agreement with this observation, as we detected substantial expression of astroglia markers *GFAP*, *S100β*, *AGT*, and *AQP4* (Figure S6). It is plausible that the progressive electrical maturation of COs during this developmental period could be driven in part by the expansion of astrocytes as these cell types have been shown to promote the functional maturation of cortical neurons *in vivo* and *in vitro* (Kuijlaars et al., 2016; Sloan et al., 2017).

The inhibitory marker GABA was initially apparent at very low levels at day 40 and increased significantly as GABAergic neurons appeared in later-stage COs, from day 60 to day 120 (Figures 3B, 4H, 4O, and S3A). To complement these analyses, we stained for the glutamatergic neuronal marker vesicular glutamate transporter 1 (VGLUT1), and observed the typical punctate staining pattern indicating the presence of this excitatory pre-synaptic marker (Figure 4I). At day 86, a large increase in SATB2$^+$ neurons was observed within expanded upper CP layers compared with day 60 COs (Figure 4E), which began to more clearly define upper and deeper CP layers (Figure 4J). Thus, it is probable that our MEA recordings at days 64 and 99 comprise electrical activities arising from CR and CTIP2$^+$ and SATB2$^+$ neurons, whereas day 120 and 161 recordings also include the electrical activities of

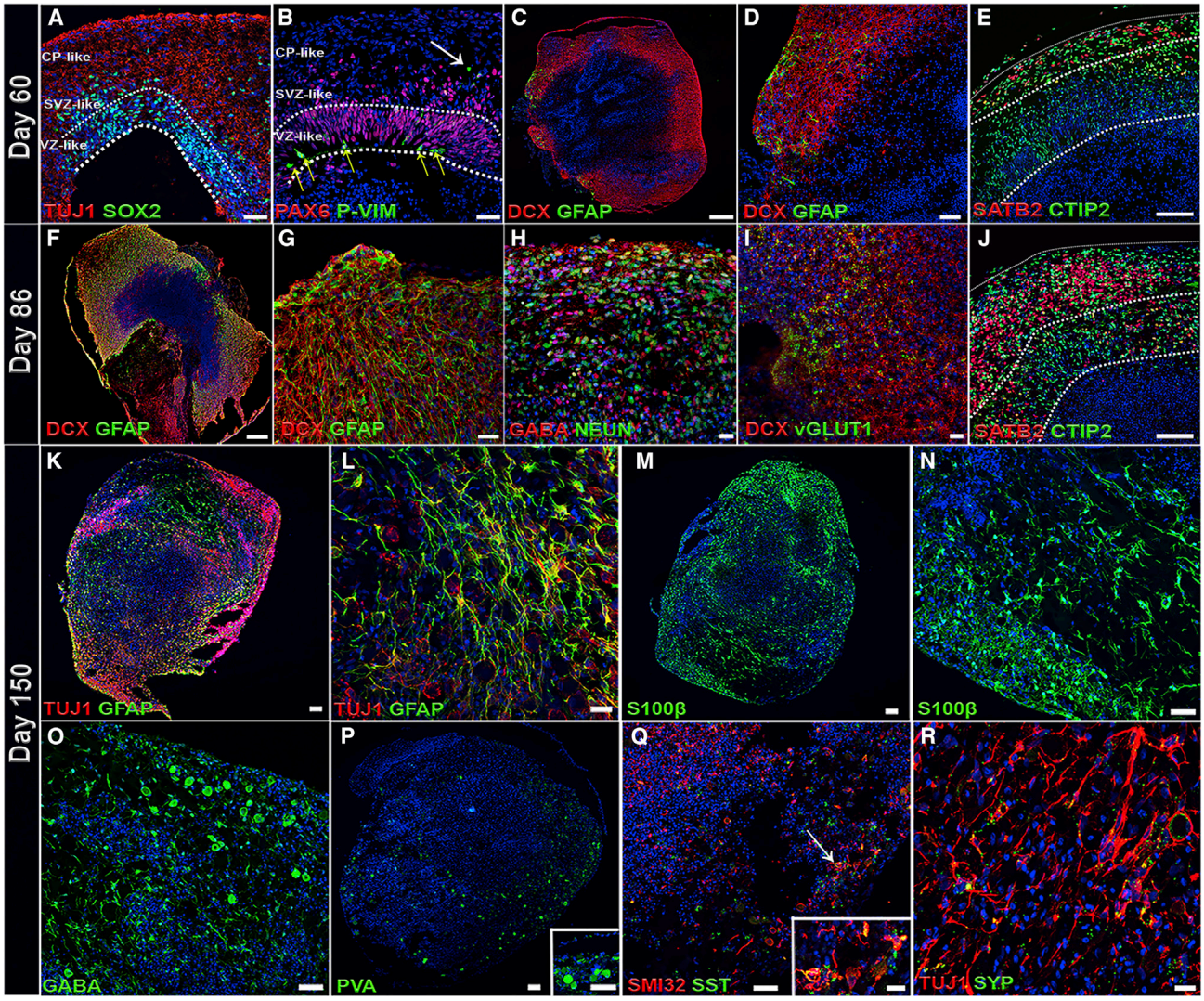

Figure 4. Cell-Type Diversity in COs

(A) Immunostaining of day 60 COs shows SOX2$^+$ NPCs lining the ventricle-like structures within COs. At day 60, the majority of SOX2$^+$ NPCs are restricted to the VZ-like areas within the area of dashed lines. SOX2$^+$ NPCs are also observed migrating into SVZ-like areas and rarely observed in CP-like zones as shown by TUJ1 immunostaining at this developmental stage. Scale bar, 50 μm.

(B) Immunostaining for the radial glial (RG) marker PAX6, showing dense expression primarily within the VZ-like area, in addition to the mitotic RG marker phospho-Vimentin (P-VIM), showing RG preferentially dividing at the apical surface (yellow arrows, lower dashed line). PAX6$^+$ RGs observed outside of the VZ-like zone representbasal RG cells, which also remain mitotically active to a lesser extent, as shown by P-VIM staining (white arrow). Scale bar, 50 μm.

(C) Day 60 COs show the emergence of astroglia as shown by GFAP staining. DCX, a neuronal migratory marker, demarcates the CP-like zone. Scale bar, 200 μm.

(D) High-magnification image of (E) showing the presence of GFAP$^+$ astrocytes. Scale bar, 50 μm.

(E) Immunostaining for the late-born and superficial CP marker SATB2 and the deep-layer CP marker CTIP2. Dashed lines indicate upper SATB2$^+$ cortical layer zone with deeper layer CTIP2$^+$ zone. Scale bar,100 μm.

(F) Day 86 COs show significant expansion of GFAP$^+$ astrocytes within the CP-like zone, which also contains DCX$^+$ neurons. Scale bar, 200 μm.

(G) High-magnification image of (I) showing the increased presence of GFAP$^+$ astrocytes compared with day 60. Scale bar, 50 μm.

(H) Immunostaining for the inhibitory neuronal marker GABA and the mature neuronal marker NEUN. Scale bar, 20 μm.

(I) Presence of excitatory neurons is also observed as shown by staining for the vesicular glutamate transporter 1, vGLUT1, which co-localized with DCX in the CP-like zone. Scale bar, 50 μm.

(legend continued on next page)

GABAergic neurons. These data, which are consistent with previous reports, indicate that whole-brain COs can develop for an extended duration in culture and generate diverse brain cell lineages.

COs Exhibit a Diversity of Apical and Basal Radial Glial Subtypes

Next, we examined whether our whole-brain COs generated the diversity of RG cell types that are present in the developing human brain. Given the instrumental role that apical radial glia (aRG) and bRG play in the structural scaffold and maturation of the developing human brain, we first confirmed their presence in the transcriptome of late-stage COs with our scRNA-seq data (Figure 5). We observed substantial RG marker expression in both the glia and the proliferative progenitor clusters (Figure 5D), including the aRG markers *ANXA1*, *PALLD*, and *CRYAB*; the late bRG markers *HOPX* and *FAM107A*; and the pan-radial glia markers *SOX2* and *PAX6* (Thomsen et al., 2016). We also noted a remarkable increase in the anti-proliferative and pro-neurogenic *BTG2* (also known as *TIS21*) from day 93 to day 140 (Figure 5D), which indicates a significant increase in progenitor division fates destined to become neurons (Attardo et al., 2010; Iacopetti et al., 1999). We then characterized their development from day 60 to day 140 by IHC. At day 60, we noted pVIM$^+$ mitotic RG cells within VZ-like and radially distant, SVZ-like regions comprising early progenitors found in the scaffold of the embryonic brain (Figure 4B). At day 90, the VZ- and SVZ-like regions primarily contained SOX2$^+$/HOPX$^+$ progenitors (Figures S6A–S6C). By day 140, CRYAB$^+$ progenitors appeared at the apical surface, whereas HOPX$^+$ progenitors appeared in a distant outer VZ-like zone (Figures 5A and 5B). This patterning suggests that COs contain regionally defined aRG and bRG populations that become readily apparent by day 140. Recently, a study described the emergence of truncated radial glia (tRG) that marks the beginning stages of the transition from a continuous to a discontinuous RG scaffold in late human brain development (Di Lullo and Kriegstein, 2017; Nowakowski et al., 2016). tRG, which express the CRYAB marker, are formed when aRG retract their basal fibers and terminate them in the outer SVZ, thus resembling a truncated morphology. Interestingly, we identified CRYAB$^+$ progenitors in COs, although future studies are necessary to further validate whether they represent tRG as observed *in vivo*.

Neuronal and Synaptic Maturation in COs

Neuronal and synaptic development is indispensable to the formation of neural circuits and drives EP maturation of COs. Therefore, we sought to identify evidence of this maturation at the protein and transcriptome levels around days 120–150 in culture. We first noted the formation of synapses in day 120 COs with expression of the mature pre-synaptic marker synaptophysin (SYP) that partially co-localized with the mature neuronal dendritic marker MAP2 (Figure S4A). We further examined the expression levels of a more comprehensive gene panel of dendritic, presynaptic, and postsynaptic markers in our scRNA-seq data in day 140 COs (Figure S4B). We evaluated synaptic markers enriched within either inhibitory or excitatory neurons. These markers may be critical for synaptic propagation, as they correlate with the increased spiking activity and SBF that we detected in late-stage COs. For example, *GAP43*, *SYT4*, *SYP*, and *SLC17A7* (Figure S4B, highlighted) are pre-synaptic markers enriched in excitatory neurons. Conversely, *NRXN3* and *SLC32A1* (Figure S4B, highlighted) are pre-synaptic markers enriched in inhibitory neurons. In some cases, these genes encode well-documented functions for these classes of neurons. For example, *SLC17A7* encodes vesicular glutamate transporter 1 (*VGLUT1*) and *SLC32A1* encodes for VIAAT, which is a membrane protein associated with the uptake of GABA and glycine into synaptic vesicles. In addition to pre-synaptic markers, we also observed expression of the post-synaptic marker *HOMER1*, *GPHN*, *NLGN1*, *NLGN2*, *DLG3*, *DLG4* (also known as PSD95), and *SHANK* gene family members in both neuronal classes, although most markers showed enrichment in excitatory neurons.

Given this evidence of synaptic maturation, we extended our analyses in day 150 COs for additional support of neuronal maturation. Of note, we observed a significant increase in GFAP$^+$ and S100β$^+$ astrocytes by day 150 in culture (visualized in Figures 4K–4N, quantified in S3A). These astrocytes exhibited extensive, ramified processes that indicate their maturation and association with neuronal populations (Figures 4K–4N). We also found that from day 86 to day 150, our COs exhibited significantly

(J–N) (J) Day 86 COs show an expansion of the superficial SATB2$^+$ cortical layer zone compared with day 60 COs. Dashed lines indicate more defined upper SATB2$^+$ cortical layer zone and deeper layer CTIP2$^+$ zone. Scale bar, 100 μm. (K–N) Immunostaining of day 150 cerebral COs shows presence of neuronal (K and L, TUJ1) and astrocytic cell lineages (K and L, GFAP, and M and N, S100β). Scale bars, (K and M) 100 μm, (L) 20 μm, and (N) 50 μm.

(O–R) Maturation of day 150 COs exhibits GABAergic neurons as shown by (O) GABA staining and interneuron subtypes, (P) parvalbumin (PVALB), and (Q) somatostatin (SST). Scale bars, (O) 50 μm; (P) 100 μm and inset, 50 μm; (Q) 50 μm and inset, 25 μm. (R) Synaptic maturation is also observed in day 150 COs as shown by expression of the pre-synaptic marker, synaptophysin (SYP). Scale bar, 25 μm. All images were stained with DAPI (blue) (n = 4 independent organoids, all time points).

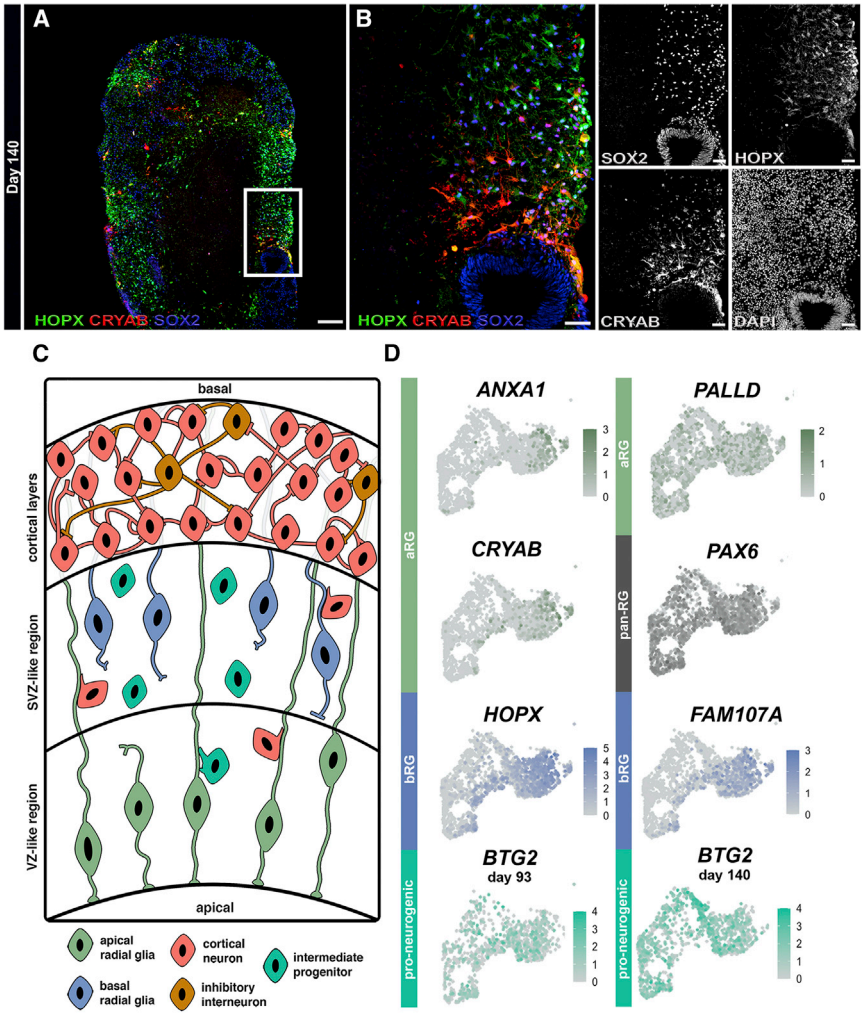

Figure 5. Presence of Diverse RG Cells in COs

(A) Low-power composite image of HOPX, CRYAB, and SOX2 expression in day 140 COs. White frame indicates reference for (B).

(B) High-power merged and single-channel images from inset in (A).

(C) Schematic depicting progenitor zones in the CO model.

(D) Feature UMAPs of integrated glia and proliferative progenitor clusters (note the retained shape of clusters from Figure 3). From top to bottom: expression of aRG-specific markers *PALLD*, *ANXA1*, and *CRYAB*; bRG-specific markers *HOPX* and *FAM107A*; pan-RG markers *PAX6* and *SOX2* in integrated scRNA-seq dataset; and anti-proliferative/pro-neurogenic marker *BTG2* shows increased expression over time (left, day 93, and right, day 140) (n = 4 independent organoids). Scale bar (A), 200 μm. All scale bars in (B), 50 μm.

increased levels of GABA expression (visualized in Figure 4O, quantified in Figure S3A). GABAergic neurons in day 150 COs showed significantly larger cell bodies compared with those in earlier-stage COs (Figure 4O). We were able to identify specific GABAergic neuron subtypes, including those that were immunoreactive to either parvalbumin or somatostatin, which further provides evidence for GABAergic neuron maturation (Figures 4P and 4Q). Finally, we noted the pan-neuronal marker TUJ1 to localize with the pre-synaptic marker SYP, which depicts the development of mature CO networks (Figure 4R).

Gene Expression Profiling in Mature COs Reveals Activation of the NTR/Trk Receptor Signaling Pathway

To further investigate whether the observed EP maturation of COs correlated with concomitant changes in gene expression patterns, we performed qRT-PCR and profiled the expression of 84 key genes associated with human synaptic plasticity at three additional time points during CO development (day 10, day 60, and day 150) (Figure 6). For this analysis, we selected a wide range of time points to identify synaptic gene expression changes that more clearly delineated immature (day 60) from mature (day 150) neuroelectrical properties in COs. As shown in Figure 6A, these genes encode a diverse set of protein functions that are associated with synaptic activity and were functionally categorized into 10 groups, such as neuronal receptors, cell adhesion molecules, or immediate-early response gene (IEG) groups. Genes that were upregulated 3-fold or higher relative to hiPSC gene expression levels were collated into these 10 groups and their percentage abundance was determined from each organoid time point. Interestingly, this analysis revealed increased expression of the *TRKB* receptor (Figure 6C) during organoid development without a concomitant increase in the expression of one of its ligands, BDNF. These data agree with a previous study showing that activation of TrkB in

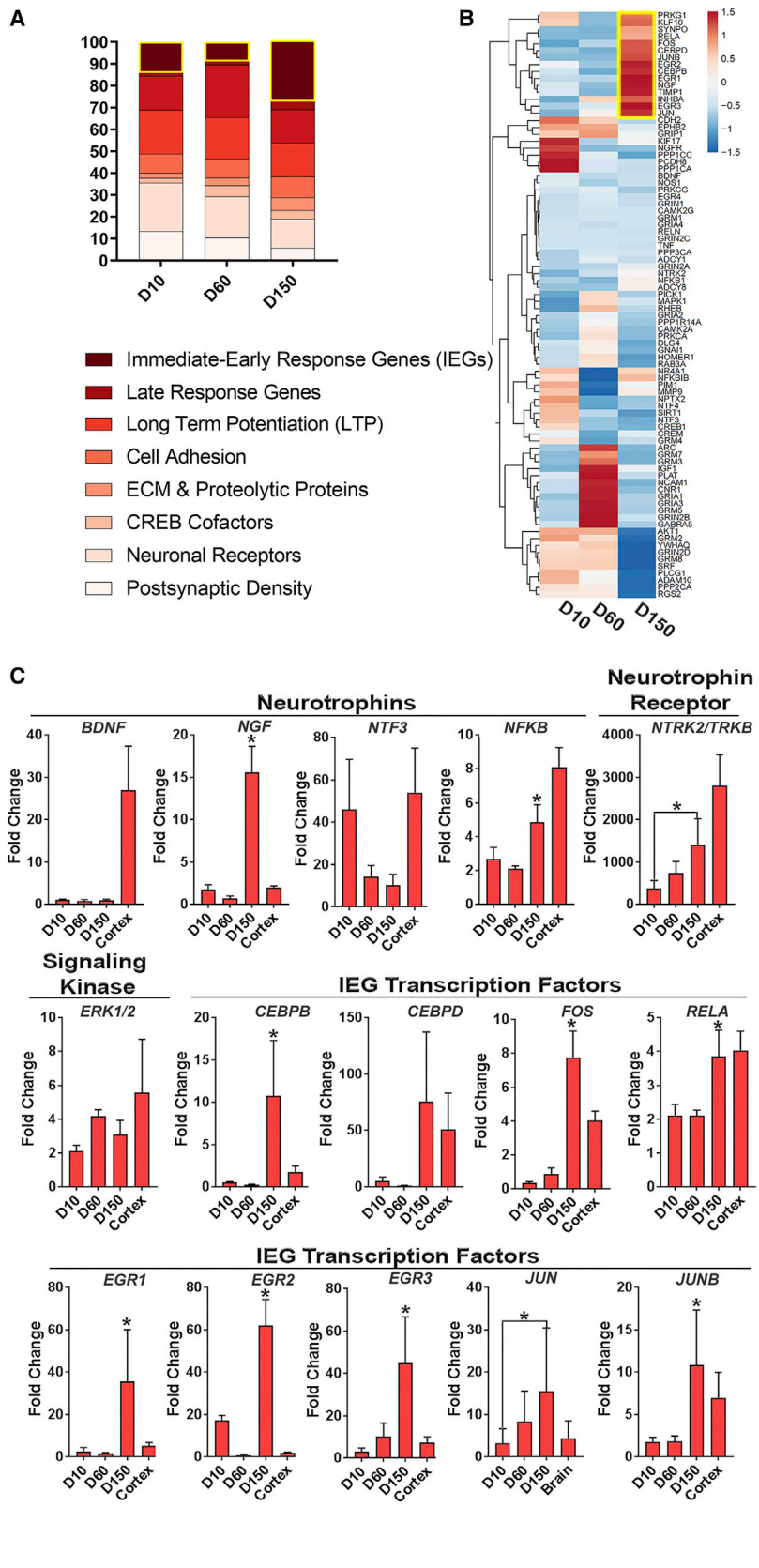

Figure 6. Gene Expression Profiling Reveals Activation of an IEG Cluster in Day 150 COs

(A) Functional categorization of upregulated genes involved in synaptic plasticity. The highlighted boxed segments in the bar graph at each time point refer to IEGs.

(B) Heatmap of gene expression dynamics associated with synaptic activity at days 10, 60, and 150 during CO development.

(C) Quantitative expression analyses of NTR/TRK signaling and IEG activation genes regulating synaptic plasticity at days 10, 60, and 150 during CO development. Profiled gene members include NTRs, the TRKB receptor, the ERK 1/2 signaling kinase, and multiple IEG transcription factors. Gene expression values that showed significant differences ($p < 0.05$) between day 60 and day 150 time points are indicated by an asterisk. Adult human brain cortex was included as a positive control (n = 5 independent organoids pooled together and 3 independent experiments performed).

newborn cortical neurons occurs through EGFR signaling rather than through BDNF, which is expressed at low levels during brain development but increases in expression after birth (Puehringer et al., 2013). In contrast, we also observed a relative increase in the levels of NGF at day 150, which may reflect the expansion of inhibitory neurons at this time point and agrees with a report demonstrating that this NTR is primarily produced in GABAergic neurons (Biane et al., 2014). In addition, in agreement with our IHC analysis, we observed an increase in AMPA/NMDA receptor expression at day 60, which signifies the maturation of excitatory neurons (Figure 6B). The relative expression of these genes appears to decrease by day 150, although this observation most likely reflects the increased population of inhibitory neurons at this time point, which artificially dilutes AMPA/NMDA expression levels (Figures 3 and S5B). We did not observe a significant change in the expression levels of these genes specifically in excitatory neurons in our scRNA-seq dataset, which supports this conclusion (Figure S5B).

In addition, 14 IEG genes were upregulated in day 150 COs (Figure S5C). IEGs have been shown to play critical roles in promoting synaptic formation, transmission, and maturity (Kim et al., 2018; Lanahan and Worley, 1998), which suggests that these genes perform similar functions to promote EP maturation in late-stage COs. Clustering analysis confirmed this finding and revealed 33 genes that were upregulated in day 150 COs that consisted of IEGs, neuronal receptor genes, postsynaptic density genes, and others. In addition, the highest upregulated gene cluster within the day 150 group comprised primarily IEGs (11/15 genes). We next determined whether these upregulated genes functioned within a common signaling pathway and used the Ingenuity Pathway Analysis (IPA) software tool to perform this bioinformatics analysis. This analysis revealed 205 canonical pathways with a default threshold ($-\log(\text{p value}) > 1.3$). We focused on those canonical pathways that were both enriched in the developing human brain and were top ranked according to their statistical significance. Based on these criteria, we identified IL17A and the NTR/TRK signaling pathway as the top two ranked canonical pathways ($-\log(\text{p value}) = 13.2$ and 13.1, respectively) (Table S2). We further verified whether the receptors mediating the activation of these downstream molecules were relevant to brain development. We noted a significant increase in the expression of the TRKB receptor at day 140 compared with day 90 (Table S2 and Figure S5E), which suggests NTR/TRK signaling is enriched as COs mature. Conversely, we did not note significant changes in the expression of IL-17RA or the related IL-17RC over time (Figure S5D and Table S4) and believe the apparent enrichment of IL17A signaling in our IPA is a reflection of its common downstream targets with the NTR/TRK signaling pathway. Taken together, these findings suggest that NTR/TRK signaling contributes to promoting synaptic maturation in COs and may drive complex network bursting activities.

DISCUSSION

COs have shown significant promise as three-dimensional model systems of human brain development and have shaped our current understanding of key neurodevelopmental milestones (Birey et al., 2017; Camp et al., 2015; Hartlaub et al., 2019; Lancaster et al., 2017; Pasca, 2018; Qian et al., 2016; Yin et al., 2016). Here we expanded upon these studies to correlate molecular and morphological features in COs with their EP trajectories. To accomplish this analysis, we used our MEA methodology to evaluate the transition of neural circuits from spontaneous activity to more robust electrical features that give rise to network bursting. This EP trajectory indicates the development of highly connected neural networks, which is reminiscent of the functional maturation of early brain development. We simultaneously characterized the morphological development of the progenitor and cortical populations that give rise to this neuroelectrical maturation with IHC and transcriptomic analyses. For instance, we found that the emergence of GABAergic neurons in our transcriptomic and IHC data from late-stage COs correlated with the onset of mature network bursting observed in our MEA data. We also noted the increased incidence of neurogenic progenitor divisions, supported by increased *BTG2* expression in the transcriptome of day 140 COs, which coincided with the rapid development of neural networks and subsequent functional maturation.

Our findings are congruent with reports by Giandomenico et al. and Trujillo et al. that describe network bursting in CO slices and intact forebrain COs, respectively. These bursting events become prominent between 4 and 6 months in culture and continue to develop nested oscillatory network events by 8–10 months in culture. The work presented here expands these findings by identifying the morphological characteristics and cellular diversity that emerge with EP maturation in whole-brain, undirected COs. It is apparent that the organoid culture conditions are pertinent to these developmental phenotypes, as we observed relatively high representation of inhibitory neurons as early as 4 months in organoid development compared with other studies (Quadrato et al., 2017; Tanaka et al., 2020; Trujillo et al., 2019).

Alternative methods that rely on calcium imaging to evaluate neuronal network activity in COs have been recently developed (Bershteyn et al., 2017; Lancaster et al., 2017; Mansour et al., 2018; Sakaguchi et al., 2019; Watanabe et al., 2017) and would greatly complement

the analyses we report here. These methods permit the quantitation of changes in intracellular calcium levels in neuronal and glial cultures (Bonifazi and Massobrio, 2019; Wong, 1998) and have been adapted for use in dissociated organoid cultures by Sakaguchi et al. The primary advantage of calcium-imaging-based methods is their ability to measure functional activity with spatial resolution. A combined approach that incorporates both calcium imaging and MEA techniques would therefore provide the advantage of analyzing functional activities with both high temporal and spatial resolution and allow a more accurate assessment of neural network dynamics in COs.

Importantly, our results highlight the translational potential of COs to model neurodevelopmental disorders that arise from aberrant neural network formation. To date, COs have provided critical insights into the structural etiology of several neurodevelopmental disorders, including autism (Hou et al., 2020; Mariani et al., 2015; Papariello and Newell-Litwa, 2020; Wang et al., 2020; Zhang et al., 2020) and epilepsy (Niu and Parent, 2020; Sun et al., 2019). However, the characterization of neural network activity is indispensable in several of these disorders, including epilepsy. The combined functional, morphological, and transcriptomic analyses of COs may be implemented to characterize the developmental trajectory of disease phenotypes. Further refinement in correlating EP properties in COs with clinically relevant measures in the neonatal brain using EEG analysis as studied by Trujillo et al. represents an important step in validating COs as a functional testing model to investigate environment and genetic insults to the neonatal brain.

In sum, our work shows that EP maturation and network activity arising in COs is coupled with dynamic developmental changes in molecular and cellular complexity. The characterization of how EP features progress in COs with their developmental properties is key in validating this model for investigating molecular and cellular mechanisms underlying neuroelectrical deficits associated with neurological disorders. As an extension to this work, this functional testing platform may be used in parallel with morphological and transcriptomic analyses to characterize disease-specific features of early brain development.

EXPERIMENTAL PROCEDURES

CO Culture

The human episomal-derived iPS-1 line was maintained under feeder-free and defined, serum-free medium conditions (Burridge et al., 2011). iPSCs were cultured in E8 medium (Thermo Fisher) and on vitronectin-coated plates. Whole-brain COs were generated according to our previously described protocol (Hester and Hood, 2017). Half of the medium within tissue culture dishes was replaced every 4 days.

MEA

Spontaneous extracellular field potentials in whole-brain COs were acquired with a 64-channel MEA system (MED64 system, Alpha MED Scientific) at a sampling rate of 20 kHz/channel and at 37°C using a temperature controller device. MEA probes (Alpha MED Scientific, MED-P515A) were treated with 0.005% polyethyleneimine and 2 μg/mL laminin prior to recording. Three-minute recordings were captured from four healthy COs per time point. COs were transferred from culture to the center of the probe containing the 8 × 8 channel array with 150 μL conditioned organoid culture medium. Spike data were imported into MED64 Mobius Offline software (version 1.4.5) and EP metrics were determined.

scRNA-seq

Approximately 10,000 live cells were used to generate scRNA-seq libraries with the 10× chromium single-cell 3′ V2 library kit (10× Genomics) according to the manufacturer's instructions, and sequencing was performed on a HiSeq 4000 System (Illumina).

Statistical Analyses

All statistical analyses were performed in GraphPad Prism v.8.1.2 or R v.3.6.1 and data are shown as the mean ± the SEM. Statistical significance was analyzed using one-way ANOVA with Tukey's multiple comparisons tests. Symbols of statistical significance were used as follows: *$p \leq 0.05$; **$p \leq 0.01$; ***$p \leq 0.001$; ****$p \leq 0.0001$. All statistical analyses of EP metrics and scRNA-seq of COs are shown in Tables S3 and S4, respectively.

See Supplemental Experimental Procedures for detailed methods for MEA (also see Table S5 for burst detection parameters), IHC, and our scRNA-seq data handling pipeline.

Data and Code Availability

The accession number for the single cell RNA sequencing data reported in this paper is GEO: GSE157019.

SUPPLEMENTAL INFORMATION

Supplemental Information can be found online at https://doi.org/10.1016/j.stemcr.2020.08.017.

AUTHOR CONTRIBUTIONS

S.R.F., D.J., A.M.H., S.T.P., G.M., T.B., and M.E.H. conceived and designed the experiments. S.R.F., D.J., A.M.H., M.E.H., S.T.P., G.M., T.L.S., E.W.H., A.B.H., W.E.A., M.A., T.B., and G.Z. performed the research. S.R.F., D.J., A.M.H., M.E.H., T.B., A.B.H., J.I., S.T.P., G.M., N.L.M., C.A.M., and I.A.B. analyzed the data. S.R.F., A.M.H., M.E.H., D.J., A.B.H., E.W.H., J.I., C.A.M., N.L.M., and I.A.B. wrote the manuscript. All authors critically reviewed and approved the final manuscript for publication. This team works in the Steve and Cindy Rasmussen Institute for Genomic Medicine at Nationwide Children's Hospital. The institute is generously supported by the Nationwide Foundation Pediatric Innovation Fund.

CONFLICTS OF INTEREST

Dr. Hester does not declare a conflict of interest related to this study. Dr. Imitola has been a consultant for Biogen and Novartis

and has received funds from Biogen for another study. All other authors do not declare a conflict of interest.

ACKNOWLEDGMENTS

We thank all laboratory members for their expert advice and constructive critiques in this study. We are also grateful to Dr. Susan Reynolds for critically reading and providing insights and edits to the manuscript and to Dr. Kathrin Meyer for providing support and guidance with the single-cell RNA sequencing experiments. This work was supported by research funds from The Abigail Wexner Research Institute at Nationwide Children's Hospital.

Received: June 20, 2019
Revised: August 28, 2020
Accepted: August 28, 2020
Published: September 24, 2020

REFERENCES

Attardo, A., Fabel, K., Krebs, J., Haubensak, W., Huttner, W.B., and Kempermann, G. (2010). Tis21 expression marks not only populations of neurogenic precursor cells but also new postmitotic neurons in adult hippocampal neurogenesis. Cereb. Cortex *20*, 304–314.

Bardy, C., van den Hurk, M., Eames, T., Marchand, C., Hernandez, R.V., Kellogg, M., Gorris, M., Galet, B., Palomares, V., Brown, J., et al. (2015). Neuronal medium that supports basic synaptic functions and activity of human neurons in vitro. Proc. Natl. Acad. Sci. U S A *112*, E2725–E2734.

Bershteyn, M., Nowakowski, T.J., Pollen, A.A., Di Lullo, E., Nene, A., Wynshaw-Boris, A., and Kriegstein, A.R. (2017). Human iPSC-derived cerebral organoids model cellular features of lissencephaly and reveal prolonged mitosis of outer radial glia. Cell Stem Cell *20*, 435–449.e34.

Biane, J., Conner, J.M., and Tuszynski, M.H. (2014). Nerve growth factor is primarily produced by GABAergic neurons of the adult rat cortex. Front. Cell. Neurosci. *8*, 220.

Birey, F., Andersen, J., Makinson, C.D., Islam, S., Wei, W., Huber, N., Fan, H.C., Metzler, K.R.C., Panagiotakos, G., Thom, N., et al. (2017). Assembly of functionally integrated human forebrain spheroids. Nature *545*, 54–59.

Bonifazi, P., and Massobrio, P. (2019). Reconstruction of functional connectivity from multielectrode recordings and calcium imaging. Adv. Neurobiol. *22*, 207–231.

Burridge, P.W., Thompson, S., Millrod, M.A., Weinberg, S., Yuan, X., Peters, A., Mahairaki, V., Koliatsos, V.E., Tung, L., and Zambidis, E.T. (2011). A universal system for highly efficient cardiac differentiation of human induced pluripotent stem cells that eliminates interline variability. PLoS One *6*, e18293.

Camp, J.G., Badsha, F., Florio, M., Kanton, S., Gerber, T., Wilsch-Brauninger, M., Lewitus, E., Sykes, A., Hevers, W., Lancaster, M., et al. (2015). Human cerebral organoids recapitulate gene expression programs of fetal neocortex development. Proc. Natl. Acad. Sci. U S A *112*, 15672–15677.

Delgado Ruz, I., and Schultz, S.R. (2014). Localising and classifying neurons from high density MEA recordings. J. Neurosci. Methods *233*, 115–128.

Di Lullo, E., and Kriegstein, A.R. (2017). The use of brain organoids to investigate neural development and disease. Nat. Rev. Neurosci. *18*, 573–584.

Felix, L., Stephan, J., and Rose, C.R. (2020). Astrocytes of the early postnatal brain. Eur. J. Neurosci. https://doi.org/10.1111/ejn.14780.

Fietz, S.A., Kelava, I., Vogt, J., Wilsch-Brauninger, M., Stenzel, D., Fish, J.L., Corbeil, D., Riehn, A., Distler, W., Nitsch, R., et al. (2010). OSVZ progenitors of human and ferret neocortex are epithelial-like and expand by integrin signaling. Nat. Neurosci. *13*, 690–699.

Godbole, G., Shetty, A.S., Roy, A., D'Souza, L., Chen, B., Miyoshi, G., Fishell, G., and Tole, S. (2018). Hierarchical genetic interactions between FOXG1 and LHX2 regulate the formation of the cortical hem in the developing telencephalon. Development *145*, dev154583.

Hansen, D.V., Lui, J.H., Parker, P.R., and Kriegstein, A.R. (2010). Neurogenic radial glia in the outer subventricular zone of human neocortex. Nature *464*, 554–561.

Hartlaub, A.M., McElroy, C.A., Maitre, N.L., and Hester, M.E. (2019). Modeling human brain circuitry using pluripotent stem cell platforms. Front. Pediatr. *7*, 57.

Hester, M.E., and Hood, A.B. (2017). Generation of cerebral organoids derived from human pluripotent stem cells. In Stem Cell Technologies in Neuroscience. Neuromethods: Springer Protocols, 126, A. Srivastava, E. Snyder, and Y. Teng, eds. *(Humana Press), pp. 123–134*.

Hou, P.S., hAilin, D.O., Vogel, T., and Hanashima, C. (2020). Transcription and beyond: delineating FOXG1 function in cortical development and disorders. Front. Cell. Neurosci *14*, 35.

Iacopetti, P., Michelini, M., Stuckmann, I., Oback, B., Aaku-Saraste, E., and Huttner, W.B. (1999). Expression of the antiproliferative gene TIS21 at the onset of neurogenesis identifies single neuroepithelial cells that switch from proliferative to neuron-generating division. Proc. Natl. Acad. Sci. U S A *96*, 4639–4644.

Johnson, M.B., Wang, P.P., Atabay, K.D., Murphy, E.A., Doan, R.N., Hecht, J.L., and Walsh, C.A. (2015). Single-cell analysis reveals transcriptional heterogeneity of neural progenitors in human cortex. Nat. Neurosci. *18*, 637–646.

Kim, S., Kim, H., and Um J, W. (2018). Synapse development organized by neuronal activity-regulated immediate-early genes. Exp. Mol. Med. *50*, 11.

Kizner, V., Fischer, S., and Naujock, M. (2019). Multielectrode array (MEA)-Based detection of spontaneous network activity in human iPSC-derived cortical neurons. Methods Mol. Biol. *1994*, 209–216.

Kuijlaars, J., Oyelami, T., Diels, A., Rohrbacher, J., Versweyveld, S., Meneghello, G., Tuefferd, M., Verstraelen, P., Detrez, J.R., Verschuuren, M., et al. (2016). Sustained synchronized neuronal network activity in a human astrocyte co-culture system. Sci. Rep. *6*, 36529.

Lanahan, A., and Worley, P. (1998). Immediate-early genes and synaptic function. Neurobiol Learn Mem. *70*, 37–43.

Lancaster, M.A., Corsini, N.S., Wolfinger, S., Gustafson, E.H., Phillips, A.W., Burkard, T.R., Otani, T., Livesey, F.J., and Knoblich, J.A. (2017). Guided self-organization and cortical plate formation in human brain organoids. Nat. Biotechnol. *35*, 659–666.

Lancaster, M.A., and Knoblich, J.A. (2014). Generation of cerebral organoids from human pluripotent stem cells. Nat. Protoc. *9*, 2329–2340.

Lancaster, M.A., Renner, M., Martin, C.A., Wenzel, D., Bicknell, L.S., Hurles, M.E., Homfray, T., Penninger, J.M., Jackson, A.P., and Knoblich, J.A. (2013). Cerebral organoids model human brain development and microcephaly. Nature *501*, 373–379.

Mann, E.O., and Paulsen, O. (2007). Role of GABAergic inhibition in hippocampal network oscillations. Trends Neurosci. *30*, 343–349.

Mansour, A.A., Goncalves, J.T., Bloyd, C.W., Li, H., Fernandes, S., Quang, D., Johnston, S., Parylak, S.L., Jin, X., and Gage, F.H. (2018). An in vivo model of functional and vascularized human brain organoids. Nat. Biotechnol. *36*, 432–441.

Mariani, J., Coppola, G., Zhang, P., Abyzov, A., Provini, L., Tomasini, L., Amenduni, M., Szekely, A., Palejev, D., Wilson, M., et al. (2015). FOXG1-Dependent dysregulation of GABA/glutamate neuron differentiation in autism spectrum disorders. Cell *162*, 375–390.

Mehta, S.R., Tom, C.M., Wang, Y., Bresee, C., Rushton, D., Mathkar, P.P., Tang, J., and Mattis, V.B. (2018). Human Huntington's disease iPSC-derived cortical neurons display Altered transcriptomics, morphology, and maturation. Cell Rep. *25*, 1081–1096.e6.

Niu, W., and Parent, J.M. (2020). Modeling genetic epilepsies in a dish. Dev. Dyn. *249*, 56–75.

Nowakowski, T.J., Pollen, A.A., Sandoval-Espinosa, C., and Kriegstein, A.R. (2016). Transformation of the radial glia scaffold demarcates two stages of human cerebral cortex development. Neuron *91*, 1219–1227.

Papariello, A., and Newell-Litwa, K. (2020). Human-derived brain models: windows into neuropsychiatric disorders and drug therapies. Assay Drug Dev. Technol. *18*, 79–88.

Pasca, S.P. (2018). The rise of three-dimensional human brain cultures. Nature *553*, 437–445.

Puehringer, D., Orel, N., Luningschror, P., Subramanian, N., Herrmann, T., Chao, M.V., and Sendtner, M. (2013). EGF transactivation of Trk receptors regulates the migration of newborn cortical neurons. Nat. Neurosci. *16*, 407–415.

Qian, X., Nguyen, H.N., Song, M.M., Hadiono, C., Ogden, S.C., Hammack, C., Yao, B., Hamersky, G.R., Jacob, F., Zhong, C., et al. (2016). Brain-region-specific organoids using mini-bioreactors for modeling ZIKV exposure. Cell *165*, 1238–1254.

Quadrato, G., Nguyen, T., Macosko, E.Z., Sherwood, J.L., Min Yang, S., Berger, D.R., Maria, N., Scholvin, J., Goldman, M., Kinney, J.P., et al. (2017). Cell diversity and network dynamics in photosensitive human brain organoids. Nature *545*, 48–53.

Renner, M., Lancaster, M.A., Bian, S., Choi, H., Ku, T., Peer, A., Chung, K., and Knoblich, J.A. (2017). Self-organized developmental patterning and differentiation in cerebral organoids. EMBO J. *36*, 1316–1329.

Sakaguchi, H., Ozaki, Y., Ashida, T., Matsubara, T., Oishi, N., Kihara, S., and Takahashi, J. (2019). Self-organized synchronous calcium transients in a cultured human neural network derived from cerebral organoids. Stem Cell Reports *13*, 458–473.

Sloan, S.A., Darmanis, S., Huber, N., Khan, T.A., Birey, F., Caneda, C., Reimer, R., Quake, S.R., Barres, B.A., and Pasca, S.P. (2017). Human astrocyte maturation captured in 3D cerebral cortical spheroids derived from pluripotent stem cells. Neuron *95*, 779–790.e6.

Sousa, A.M.M., Meyer, K.A., Santpere, G., Gulden, F.O., and Sestan, N. (2017). Evolution of the human nervous system function, structure, and development. Cell *170*, 226–247.

Stiles, J., and Jernigan, T.L. (2010). The basics of brain development. Neuropsychol. Rev. *20*, 327–348.

Sun, A.X., Yuan, Q., Fukuda, M., Yu, W., Yan, H., Lim, G.G.Y., Nai, M.H., D'Agostino, G.A., Tran, H.D., Itahana, Y., et al. (2019). Potassium channel dysfunction in human neuronal models of Angelman syndrome. Science *366*, 1486–1492.

Tanaka, Y., Cakir, B., Xiang, Y., Sullivan, G.J., and Park, I.H. (2020). Synthetic analyses of single-cell transcriptomes from multiple brain organoids and fetal brain. Cell Rep. *30*, 1682–1689.e3.

Thomsen, E.R., Mich, J.K., Yao, Z., Hodge, R.D., Doyle, A.M., Jang, S., Shehata, S.I., Nelson, A.M., Shapovalova, N.V., Levi, B.P., et al. (2016). Fixed single-cell transcriptomic characterization of human radial glial diversity. Nat. Methods *13*, 87–93.

Trujillo, C.A., Gao, R., Negraes, P.D., Gu, J., Buchanan, J., Preissl, S., Wang, A., Wu, W., Haddad, G.G., Chaim, I.A., et al. (2019). Complex oscillatory waves emerging from cortical organoids model early human brain network development. Cell Stem Cell *25*, 558–569.e7.

Wang, M., Zhang, L., and Gage, F.H. (2020). Modeling neuropsychiatric disorders using human induced pluripotent stem cells. Protein Cell *11*, 45–59.

Watanabe, M., Buth, J.E., Vishlaghi, N., de la Torre-Ubieta, L., Taxidis, J., Khakh, B.S., Coppola, G., Pearson, C.A., Yamauchi, K., Gong, D., et al. (2017). Self-organized cerebral organoids with human-specific features predict effective drugs to combat zika virus infection. Cell Rep. *21*, 517–532.

Wilton, D.K., Dissing-Olesen, L., and Stevens, B. (2019). Neuron-glia signaling in synapse elimination. Annu. Rev. Neurosci. *42*, 107–127.

Wong, R.O. (1998). Calcium imaging and multielectrode recordings of global patterns of activity in the developing nervous system. Histochem. J. *30*, 217–229.

Xiang, Y., Tanaka, Y., Patterson, B., Kang, Y.J., Govindaiah, G., Roselaar, N., Cakir, B., Kim, K.Y., Lombroso, A.P., Hwang, S.M., et al. (2017). Fusion of regionally specified hPSC-derived organoids models human brain development and interneuron migration. Cell Stem Cell *21*, 383–398.e7.

Yin, X., Mead, B.E., Safaee, H., Langer, R., Karp, J.M., and Levy, O. (2016). Engineering stem cell organoids. Cell Stem Cell *18*, 25–38.

Zhang, W., Ma, L., Yang, M., Shao, Q., Xu, J., Lu, Z., Zhao, Z., Chen, R., Chai, Y., and Chen, J.F. (2020). Cerebral organoid and mouse models reveal a RAB39b-PI3K-mTOR pathway-dependent dysregulation of cortical development leading to macrocephaly/autism phenotypes. Genes Dev. *34*, 580–597.

Stem Cell Reports, Volume *15*

Supplemental Information

Electrophysiological Maturation of Cerebral Organoids Correlates with Dynamic Morphological and Cellular Development

Summer R. Fair, Dominic Julian, Annalisa M. Hartlaub, Sai Teja Pusuluri, Girik Malik, Taryn L. Summerfied, Guomao Zhao, Arelis B. Hester, William E. Ackerman IV, Ethan W. Hollingsworth, Mehboob Ali, Craig A. McElroy, Irina A. Buhimschi, Jaime Imitola, Nathalie L. Maitre, Tracy A. Bedrosian, and Mark E. Hester

Figure S1

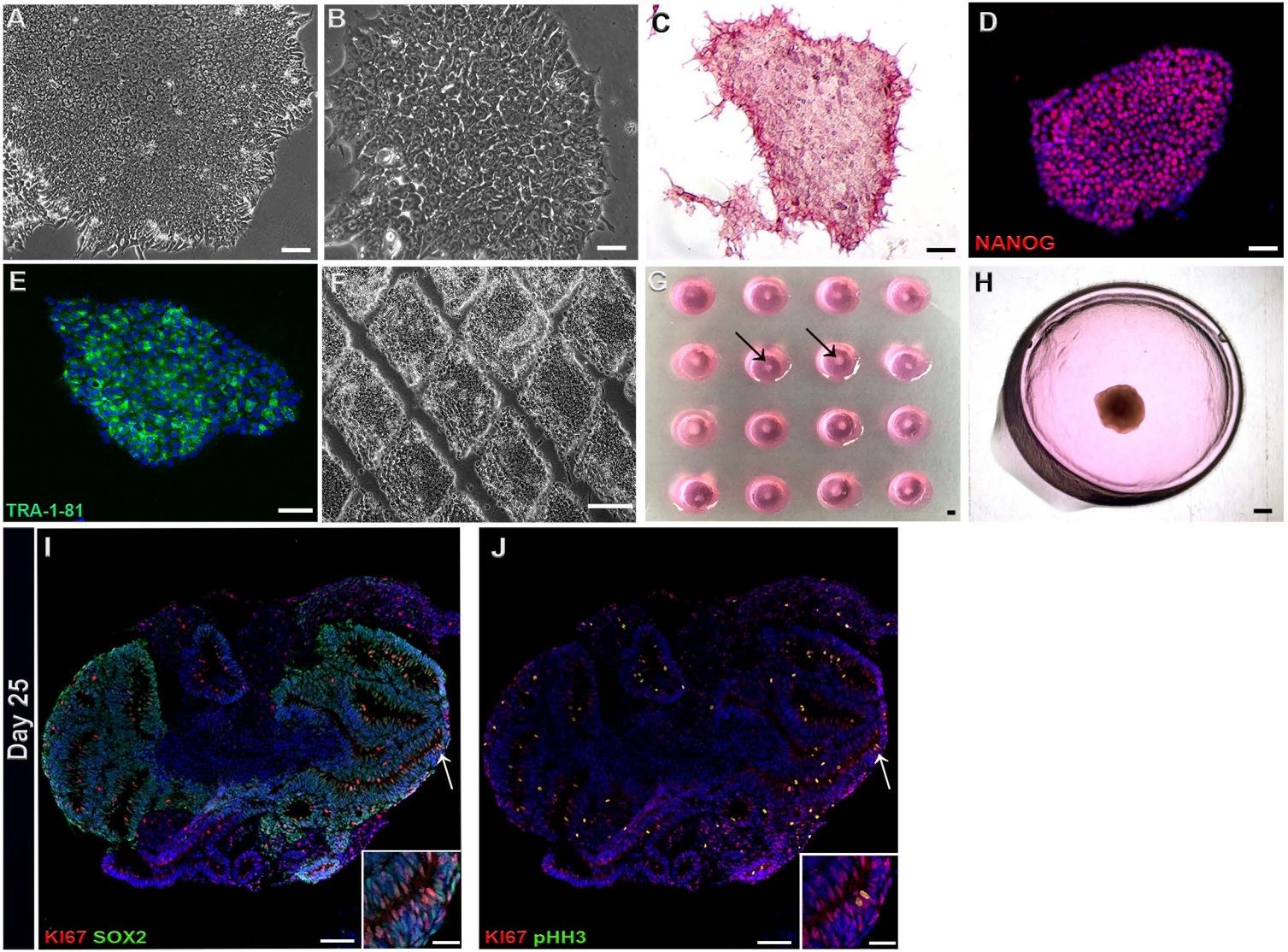

Figure S2

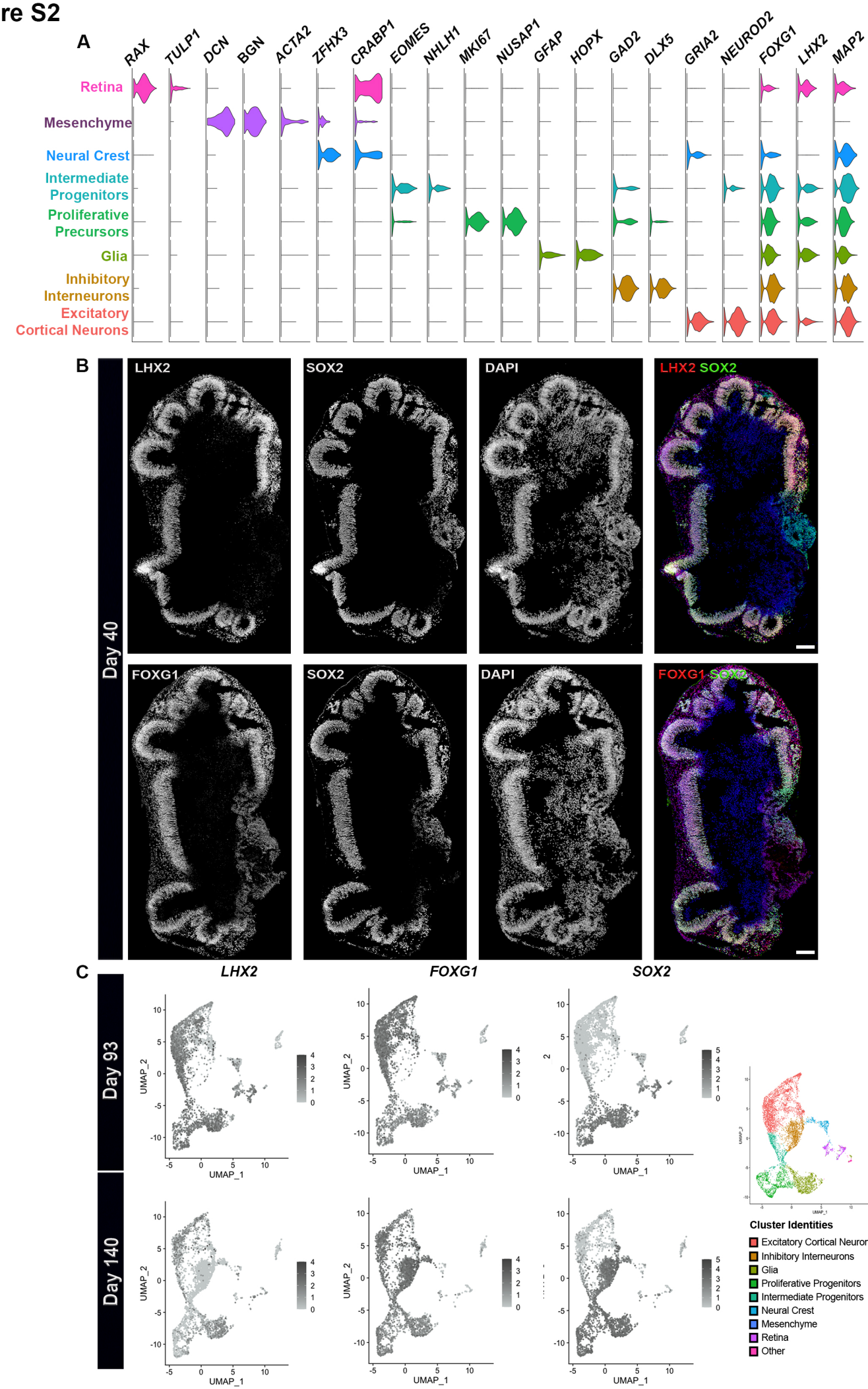
A
RAX
TULP1
DCN
BGN
ACTA2
ZFHX3
CRABP1
EOMES
NHLH1
MKI67
NUSAP1
GFAP
HOPX
GAD2
DLX5
GRIA2
NEUROD2
FOXG1
LHX2
MAP2
Retina
Mesenchyme
Neural Crest
Intermediate Progenitors
Proliferative Precursors
Glia
Inhibitory Interneurons
Excitatory Cortical Neurons
B
Day 40
LHX2
SOX2
DAPI
LHX2 SOX2
FOXG1
SOX2
DAPI
FOXG1 SOX2
C
LHX2
FOXG1
SOX2
Day 93
Day 140
UMAP_1
UMAP_2
Cluster Identities
Excitatory Cortical Neurons
Inhibitory Interneurons
Glia
Proliferative Progenitors
Intermediate Progenitors
Neural Crest
Mesenchyme
Retina
Other

Figure S3

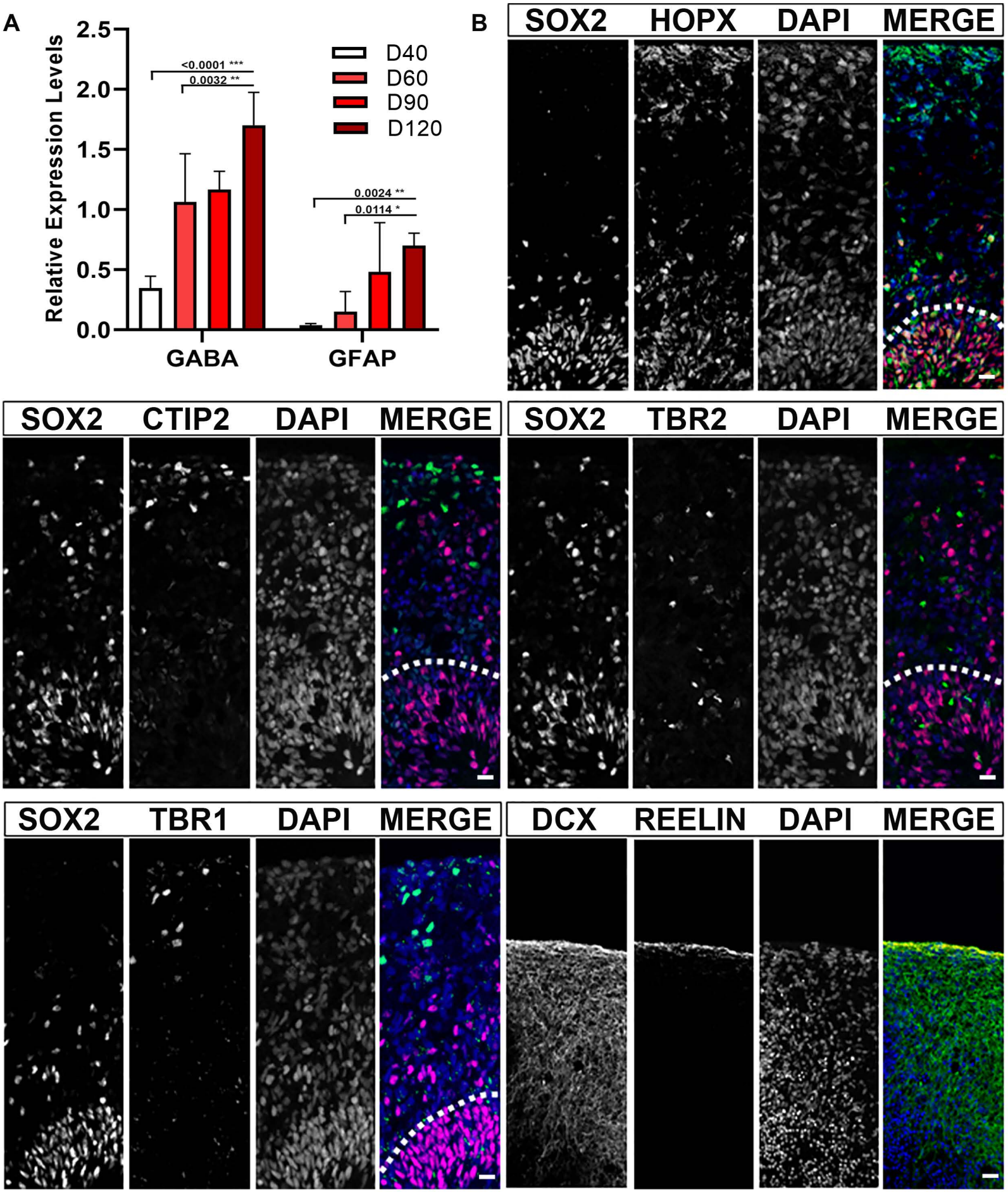
A
Relative Expression Levels
2.5
2.0
1.5
1.0
0.5
0.0
<0.0001 ***
0.0032 **
0.0024 **
0.0114 *
D40
D60
D90
D120
GABA
GFAP
B
SOX2
HOPX
DAPI
MERGE
SOX2
CTIP2
DAPI
MERGE
SOX2
TBR2
DAPI
MERGE
SOX2
TBR1
DAPI
MERGE
DCX
REELIN
DAPI
MERGE

Figure S4

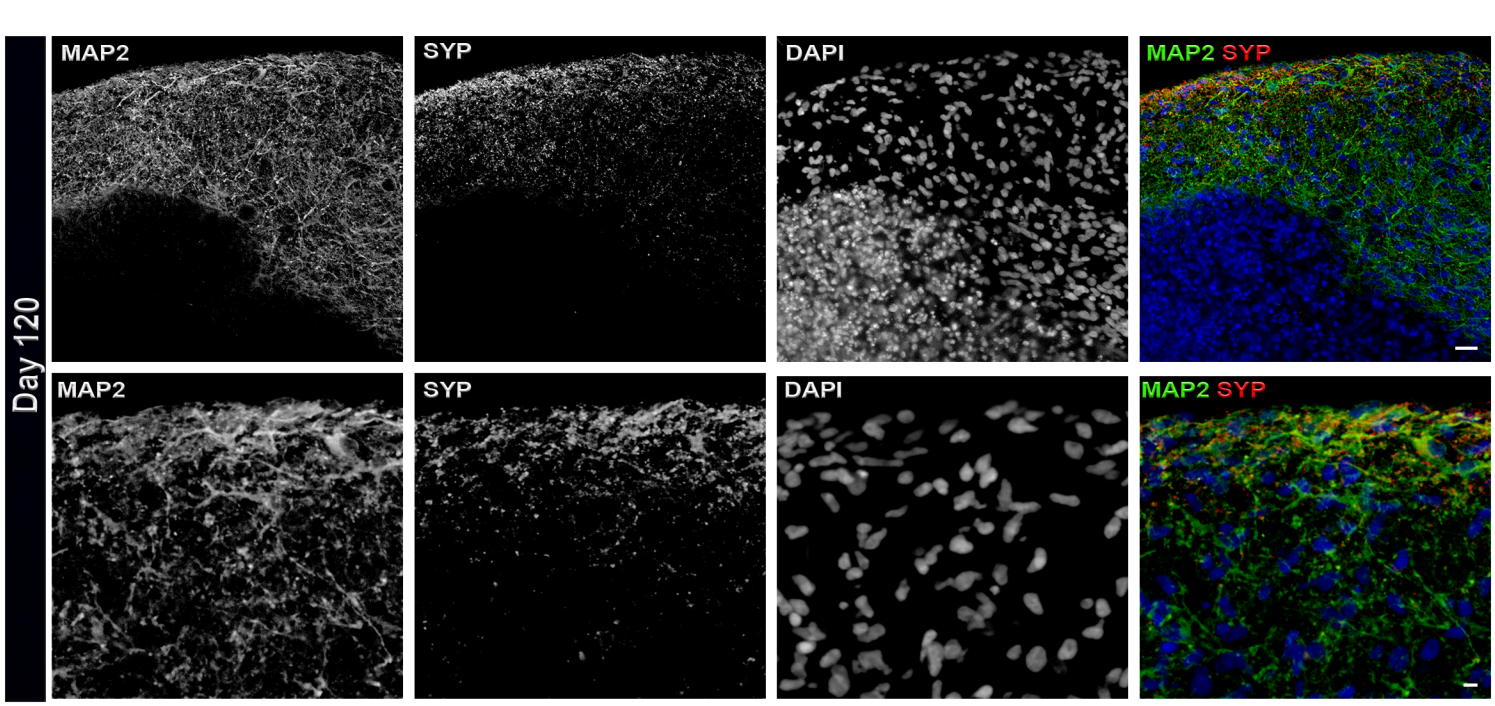
A
Day 120
MAP2
SYP
DAPI
MAP2 SYP
MAP2
SYP
DAPI
MAP2 SYP

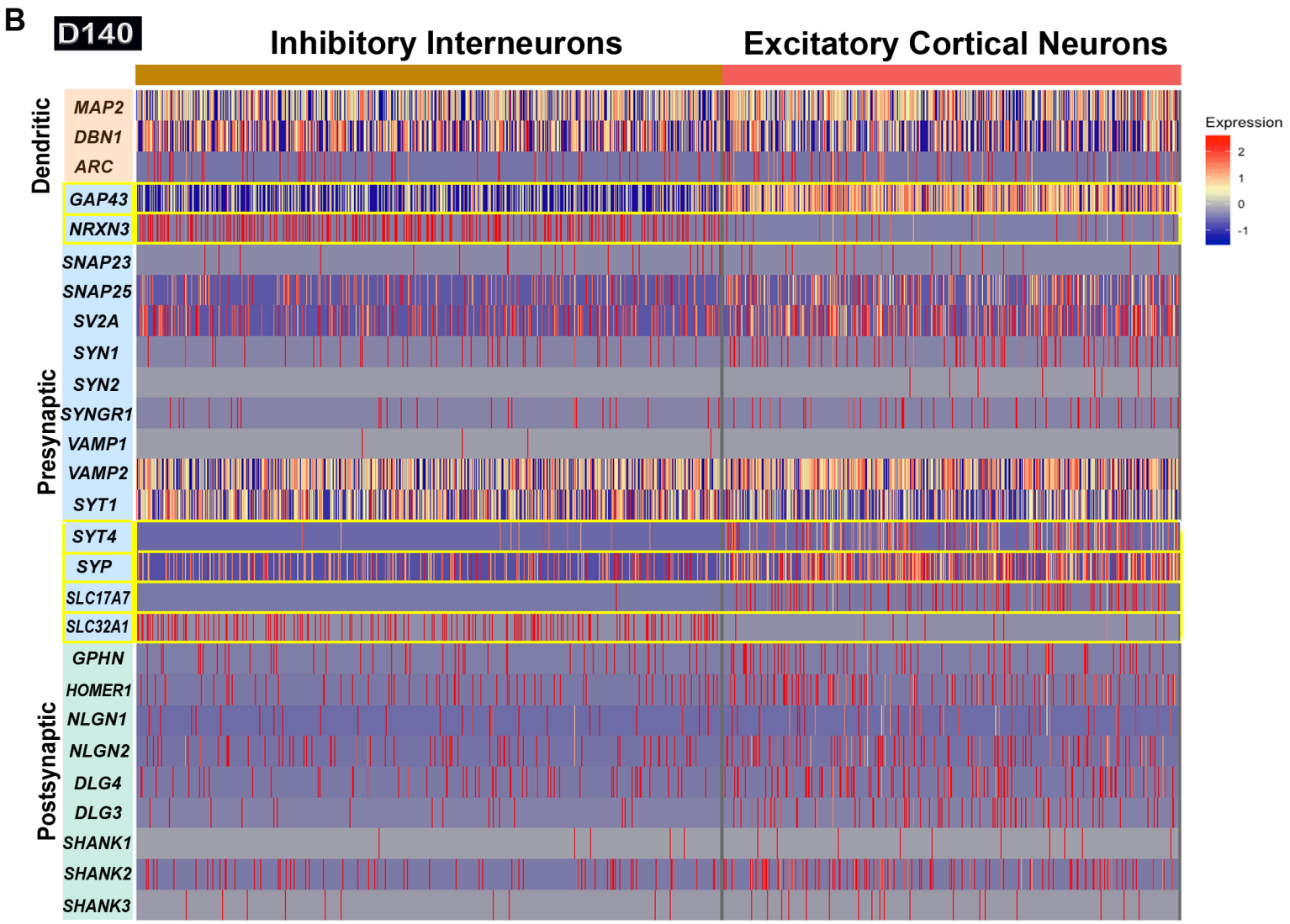
B
D140
Inhibitory Interneurons
Excitatory Cortical Neurons
Dendritic
MAP2
DBN1
ARC
GAP43
NRXN3
Presynaptic
SNAP23
SNAP25
SV2A
SYN1
SYN2
SYNGR1
VAMP1
VAMP2
SYT1
SYT4
SYP
SLC17A7
SLC32A1
Postsynaptic
GPHN
HOMER1
NLGN1
NLGN2
DLG4
DLG3
SHANK1
SHANK2
SHANK3
Expression
2
1
0
-1

Figure S5

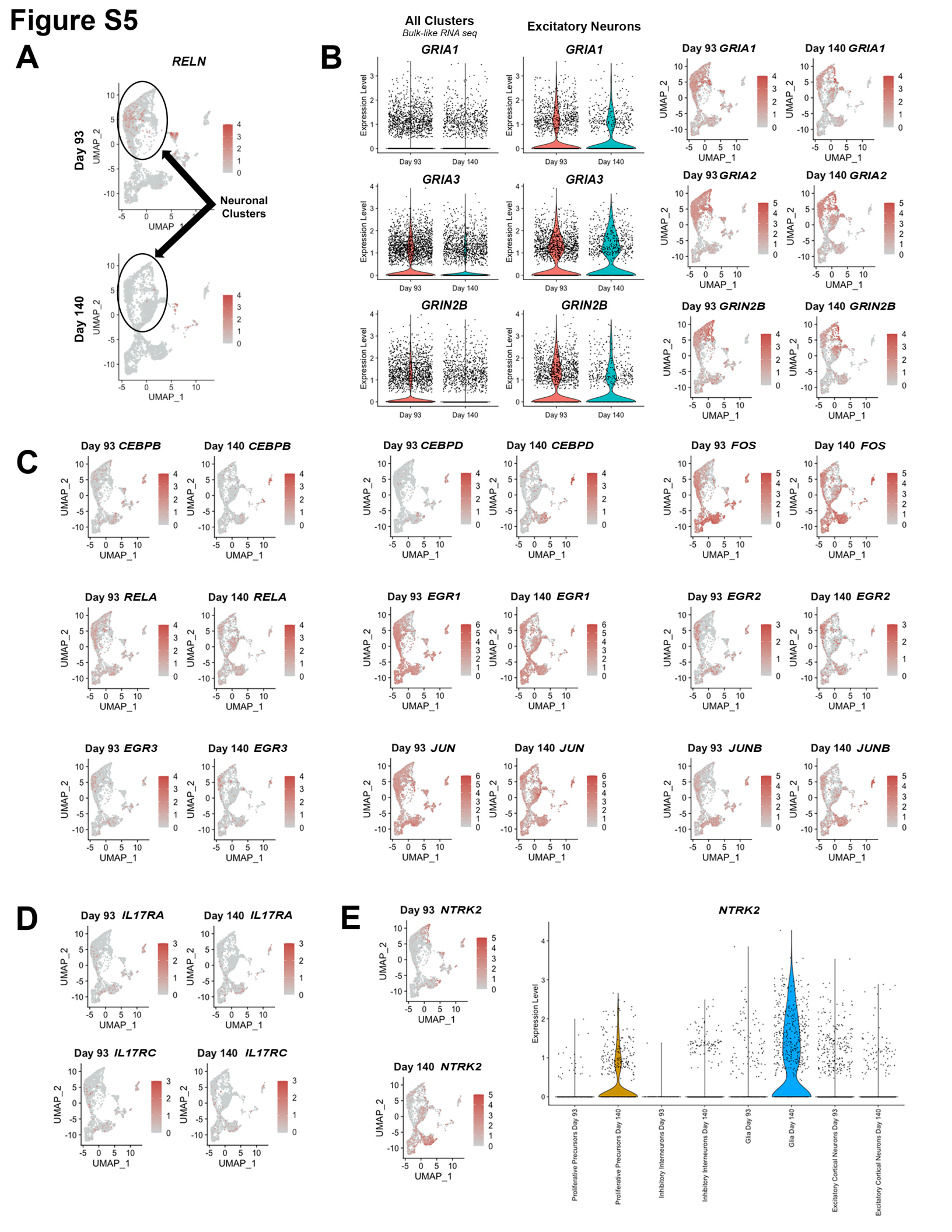
A
RELN
Day 93
Day 140
Neuronal Clusters
UMAP_1
UMAP_2
B
All Clusters
Bulk-like RNA seq
Excitatory Neurons
GRIA1
GRIA3
GRIN2B
Expression Level
Day 93
Day 140
Day 93 GRIA1
Day 140 GRIA1
Day 93 GRIA2
Day 140 GRIA2
Day 93 GRIN2B
Day 140 GRIN2B
C
Day 93 CEBPB
Day 140 CEBPB
Day 93 CEBPD
Day 140 CEBPD
Day 93 FOS
Day 140 FOS
Day 93 RELA
Day 140 RELA
Day 93 EGR1
Day 140 EGR1
Day 93 EGR2
Day 140 EGR2
Day 93 EGR3
Day 140 EGR3
Day 93 JUN
Day 140 JUN
Day 93 JUNB
Day 140 JUNB
D
Day 93 IL17RA
Day 140 IL17RA
Day 93 IL17RC
Day 140 IL17RC
E
Day 93 NTRK2
Day 140 NTRK2
NTRK2
Expression Level
Proliferative Precursors Day 93
Proliferative Precursors Day 140
Inhibitory Interneurons Day 93
Inhibitory Interneurons Day 140
Glia Day 93
Glia Day 140
Excitatory Cortical Neurons Day 93
Excitatory Cortical Neurons Day 140

Figure S6

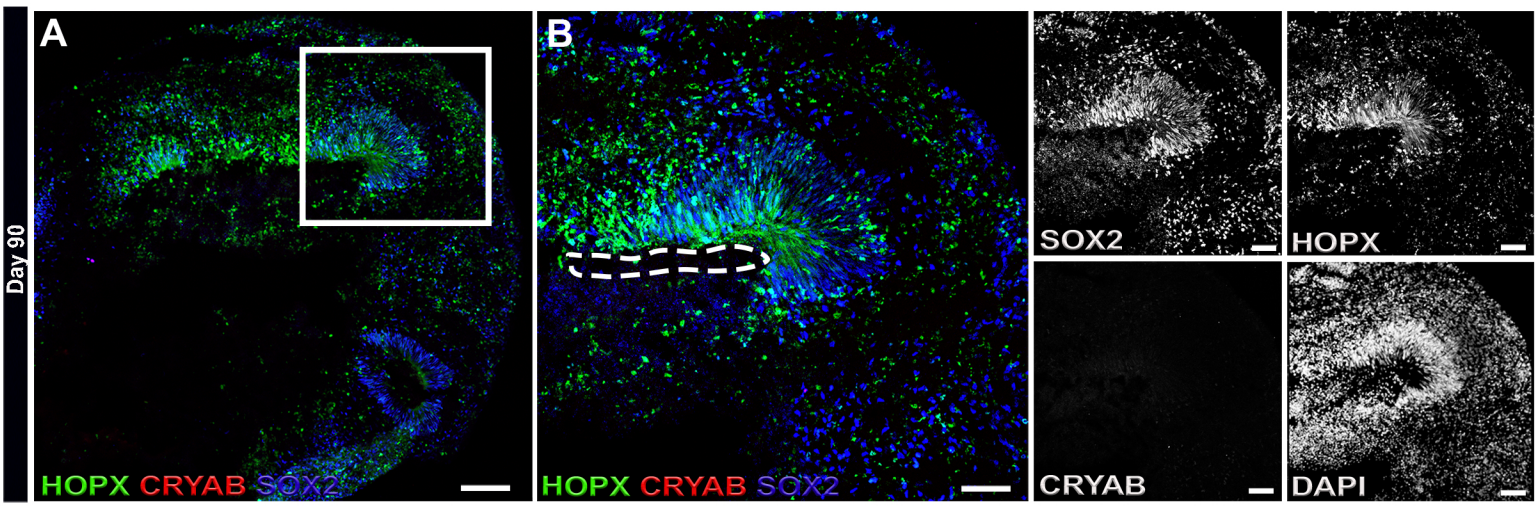
A
B
Day 90
HOPX CRYAB SOX2
HOPX CRYAB SOX2
SOX2
HOPX
CRYAB
DAPI

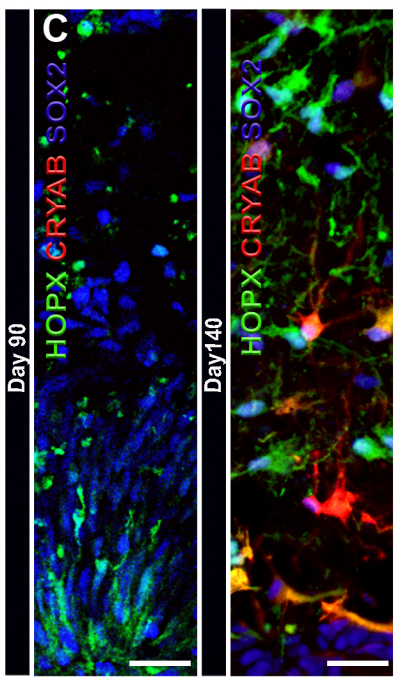
C
Day 90
HOPX CRYAB SOX2
Day140
HOPX CRYAB SOX2

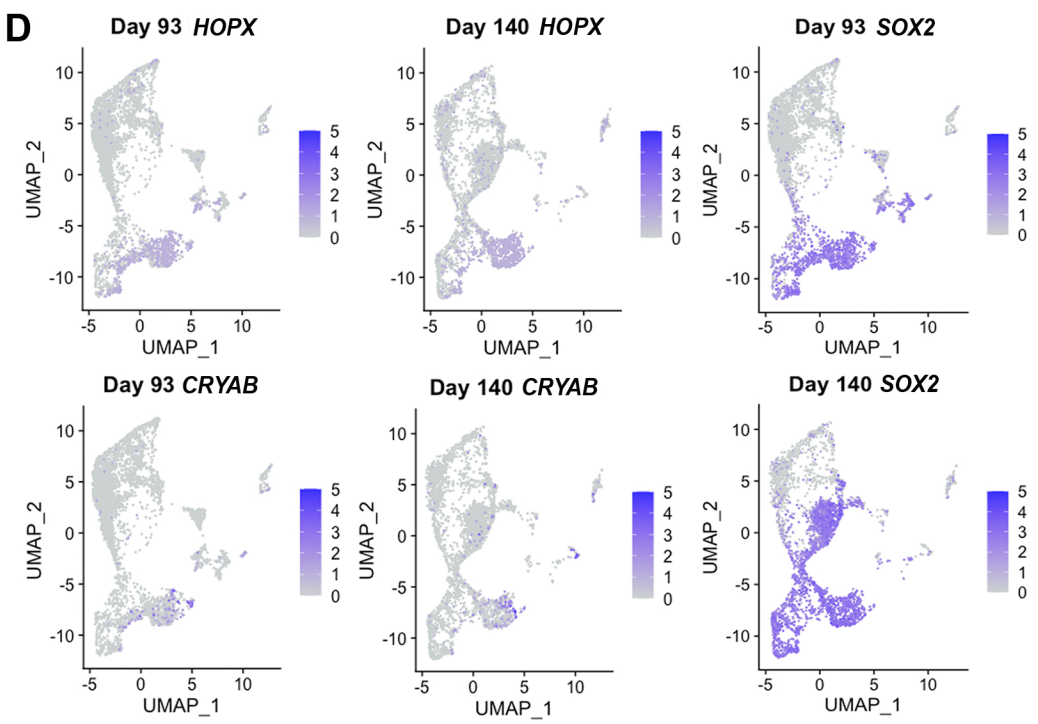
D
Day 93 HOPX
Day 140 HOPX
Day 93 SOX2
Day 93 CRYAB
Day 140 CRYAB
Day 140 SOX2
UMAP_1
UMAP_2

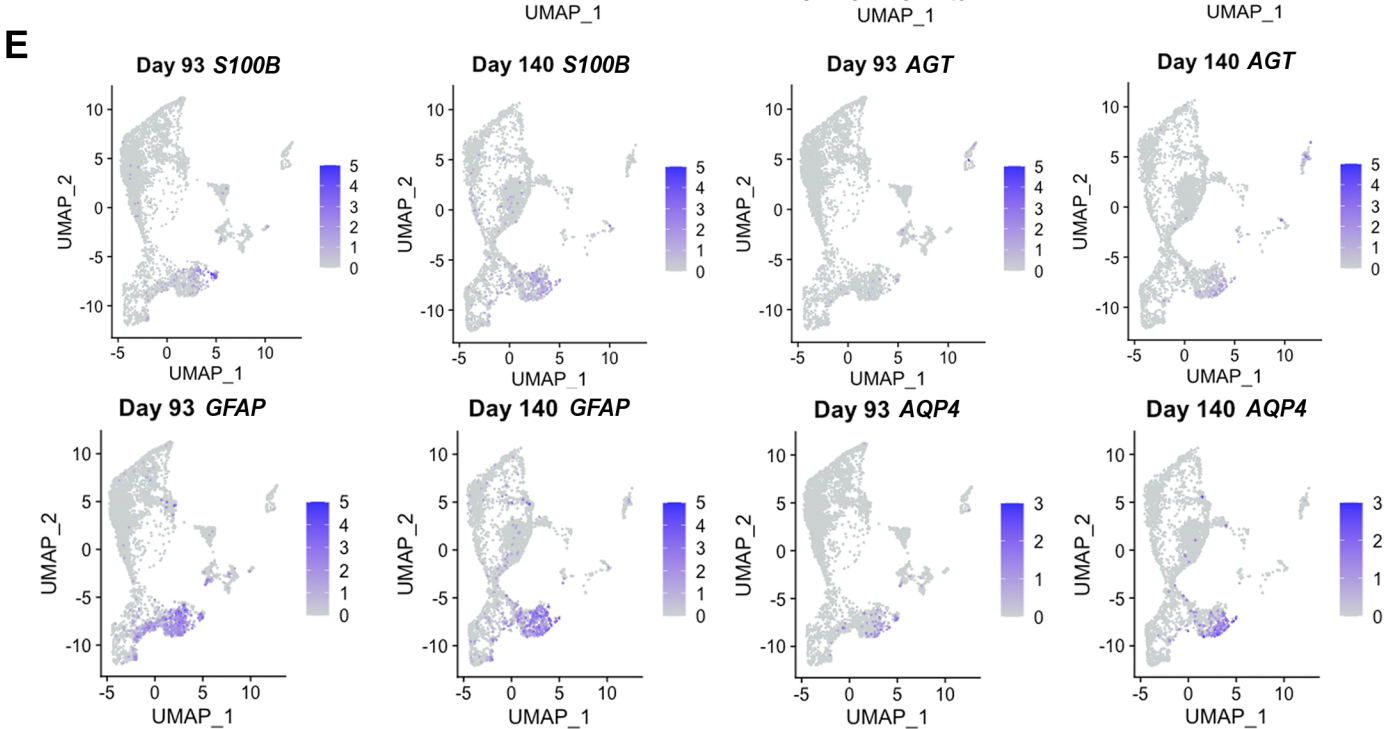
E
Day 93 S100B
Day 140 S100B
Day 93 AGT
Day 140 AGT
Day 93 GFAP
Day 140 GFAP
Day 93 AQP4
Day 140 AQP4
UMAP_1
UMAP_2

SUPPLEMENTAL FIGURE LEGENDS

Figure S1. hiPSCs Show Morphological and Molecular Features of Pluripotency and Can Develop into COs that Show Rapid NE Expansion in Early-Stages

(A-B) Phase contrast images of a hiPSC colony showing epithelial morphology and dense growth characteristics. **(C)** Image of a hiPSC colony assayed for alkaline phosphatase activity as indicted by a purple stain. **(D-E)** Immunostaining for pluripotency markers NANOG and TRA-1-81 show robust expression in hiPSCs. DAPI is shown in blue and stains all nuclei. **(F)** Phase contrast image of uniform hiPSC clusters prepared using the StemPro® EZPassage™ tool prior to embryoid body formation. **(G)** NE bodies encapsulated within the center of matrigel droplets as indicated by arrows. **(H)** Higher-magnification image of an enscapsulated NE body. **(I-J)** Immunostains of D25 COs showing rapid expansion and proliferation of SOX2+ NPCs as depicted by the proliferation marker Ki-67 and the mitosis-specific marker phospho-histone H3 (pHH3). DAPI stains nuclei in blue (n=4 organoids). SBs, panel A, 50 μm; panels (B-F, H), 100 μm; panel G, 300 μm; panels (I-J), 100μm, higher magnification inserts, 30μm.

Figure S2. Identification of Cell Clusters in COs Using Specific Gene Markers and Expansion of Neuroepithelium in D40 COs

(A) Violin plots of previously described canonical markers for all clusters. Marker genes are shown along the top horizontal axis and cell clusters are visualized along the vertical axis. **(B)** D40 COs show widespread expression of the telencephalic markers LHX2 and FOXG1 within expanding NE folds, which is co-stained with the proliferative NE marker, SOX2 (n=4 organoids). SBs, panel B, 200 μm. **(C)** Feature UMAP plots from single cell RNA sequencing data for *LHX2, FOXG1*, and *SOX2* expression in D93 and D140 COs.

Figure S3. Dynamic Gene Expression Changes and Diversity of Cortical Neuron Subtypes and Columnar Organizations

(A) Relative gene expression levels of *GABA* and *GFAP* throughout CO development, as determined by RT-PCR. **(B)** D60 COs showing representative images of immunostaining for the NPC marker SOX2 in VZ-like regions, the basal radial glial marker HOPX, and the intermediate progenitor cell marker EOMES, the cortical neuronal pre-plate marker TBR1, the cortical layer 1 marker REELIN, the neuronal migratory marker DCX and the deep layer cortical marker CTIP2. DAPI stains all nuclei and is shown in the merged image of each panel (n=4 organoids). SB in all merged images is 25 μm except for DCX and REELIN panel images where the SB is 50 μm.

Figure S4. Expression of Synaptic Gene Markers in D120 and D140 COs.

(A) IHC stains of D120 COs show MAP2+ neurons that is co-stained with the pre-synaptic marker, SYP, within COs. SB in top-panel images is 25 μm and lower panel images is 10 μm (n=4 organoids). **(B)** Heat map depicting single cell gene expression data of dendritic, presynaptic, and postsynaptic from inhibitory and excitatory neurons in D140 COs.

Figure S5. Single Cell Gene Expression Profiling in D93 and D140 COs.

(A) UMAP plots of *RELN* expression at D93 and D140. Neuronal clusters are encircled to highlight the decrease in *RELN*+ Cajal-Retzius cells by D140. **(B)** AMPA (*GRIA1*, *GRIA3*) and NMDA (*GRIN2B*) receptor expression in COs. Left to right, transcriptomic data are represented as: violin plots of total expression (i.e. bulk RNAseq-like) in all clusters, violin plots of total expression in excitatory neuron cluster only, UMAP plots of expression in all cell types at D93, and UMAP plots of expression in all cell types at D93. **(C)** UMAP plots of all IEGs mentioned in Figure 5 at D93 and D140. **(D)** UMAP plots of *IL-17RA* and *IL-17RC* at D93 and D140. (E) Left, UMAP plots of *NTRK2* at D93 and D140. Right, violin plots depicting *NTRK2* expression in all cell clusters at D93 and D140 (one independent experiment).

Figure S6. Radial Glial Marker Analysis and Single Cell Gene Expression Profiling in D93 and D140 COs.

(A) Low power composite image of HOPX, CRYAB, and SOX2 expression in D90 COs. White frame indicates reference for panel B. **(B)** High power merged and single channel images from inset in panel A. **(C)** Representative panels of radial glia organization around ventricular-like structures in D90 (left) and D140 (right) COs (n=4 organoids). **(D)** Expression of radial glia markers *CRYAB*, *HOPX*, and *SOX2* in all cell clusters at D93 and D140. **(E)** Expression of astrocyte markers *S100B*, *AGT*, *GFAP*, and *AQP4* in all cell clusters at D93 and D140. SB, panel A, 100 μm. All SBs in panel B, 50 μm. SBs, panel C, 20 μm.

Table S1. List of primary antibodies and corresponding information used for immunofluorescence studies.

Table S2. Top Canonical Pathways Enriched in D150 COs. Top-ranked canonical pathways enriched in D150 COs, as indicated by Ingenuity Pathway Analysis (IPA) software. Significance is determined by IPA's default threshold [–log (p-value)>1.3]. The number of genes associated with each canonical pathway is shown from a total of 33 differentially upregulated genes. **Denotes the pathway is associated with NTR/TRK signaling.

Table S3. Comprehensive statistical analyses of EP data as shown in Figure 3. Refer to associated excel file.

Table S4. Statistical summary data from scRNA sequencing analyses as shown in Figure S8.

Table S5. Burst detection parameters used in Mobius Offline Software.

TABLES

Table S1. List of primary antibodies and corresponding information used for immunofluorescence studies.

Antibody	Full Name	Description	Vendor	Catalog #	Species	Dilution
CRYAB	Alpha B Crystallin	Truncated radial glial (tRG) marker	Abcam	ab13496	Ms	1:300
CTIP2	COUP-TF-interacting protein 2	Deep cortical layer 5 marker	Abcam	ab18465	Rat	1:500
DCX	Doublecortin	Microtubule-associated protein associated with neuronal migration	Santa Cruz	sc-8066	Gt	1:200
FOXG1	Forkhead Box G1	Dorsal forebrain marker	Abcam	ab18259	Rb	1:1000
GABA	γ-aminobutyric acid	Major inhibitory neurotransmitter in the CNS	Sigma	A2052	Rb	1:500
GFAP	Glial fibrillary acidic protein	Astrocyte marker	DAKO	Z033429-2	Rb	1:300
HOPX	HOP Homeobox	Outer radial glia marker	Santa Cruz	sc-30216	Rb	1:1000
KI67	Proliferation Marker Protein Ki-67	Marker of all active phases of the cell cycle (G1, SG2, M)	Abcam	ab15580	Rb	1:200
LHX2	LIM Homeobox 2	Dorsal forebrain marker	Abcam	ab184337	Rb	1:200
MAP2	Microtubule Associated Protein 2	Mature neuronal, dendritic marker	Millipore	AB5622	Rb	1:300
NANOG	Homeobox Transcription Factor Nanog	Pluripotency marker	R&D Sys.	AF1997	Gt	1:200
NEUN	Neuronal nuclei	Nuclear localized, mature neuronal marker	Millipore	MAB377	Ms	1:500
PAX6	Paired Box Homeotic Gene-6	Ventricular radial glial marker/forebrain marker	Biolegend	901301	Rb	1:300
pHH3	Phospho-Histone H3	M-phase specific proliferation marker	Millipore	06-570	Rb	1:500
PVA	Parvalbumin	Ca2+-binding, cortical GABAergic interneuron marker	Swant	PV27	Rb	1:300
P-VIMENTIN	Phosphorylated Vimentin	Dividing radial glial (RG) marker	MBL	D076-3S	Ms	1:1000
RELN	Reelin	Marginal zone/cortical layer 1 marker	Millipore	MAB5366	Ms	1:300
S100 Beta	S-100 calcium-binding protein, beta chain	Glial specific marker expressed by a subtype of mature astrocytes.	Sigma	s26-44	Rb	1:300
SATB2	Special AT-rich sequence-binding protein 2	Superficial, late-born cortical layer II-IV marker	Abcam	ab51502	Ms	1:300
SMI32	clone SMI-32, non-phosphorylated neurofilament H	Neural axonal marker	Millipore	NE1023	Ms	1:1000
SOX2	SRY-Box 2	Neural progenitor cell marker	Santa Cruz	sc-17320	Gt	1:200
SST	Somatostatin	Neuropeptide that is specific to a class of cortical GABAergic interneuron subtype	Santa Cruz	sc-74556	Rb	1:300
SYP	Synaptophysin	Pre-synaptic neural marker	Millipore	MAB329	Ms	1:1000
TBR1	T-Box, Brain 1	Early born, pre-plate cortical marker	Abcam	Ab31940	Rb	1:500
TBR2	T-Box, Brain 2	Intermediate progenitor (IP) marker	Abcam	Ab23345	Rb	1:300
TRA-1-81	Podocalyxin	Surface protein expressed on human pluripotent stem cells	Thermo-Fisher	41-1100	Ms	1:200
TUJ1	Neuron-specific Class III β-tubulin	Immature neural marker	Biolegend	801201	Ms	1:500
VGLUT1	Vesicular glutamate transporter 1(SLC17A7)	Glutamatergic (excitatory) neural marker	Millipore	MAB5502	Ms	1:300

Table S2. Top Canonical Pathways Enriched in D150 COs. Top canonical pathways enriched in D150 COs and associated [–log (p-value). Significance is determined by IPA's default threshold [–log (p-value)>1.3]. The number of genes associated with each canonical pathway is shown from a total of 33 differentially upregulated genes. **Denotes the pathway is associated with NTR/TRK signaling.

Canonical Pathways	-log(p-value)	Associated Number of Genes (from a total of 33)
1.) IL-17A Signaling in Fibroblasts	13.2	7
2.) **Neuropathic Pain Signaling In Dorsal Horn Neurons	13.1	9
3.) Synaptic Long Term Potentiation	10.9	8
4.) IL-17A Signaling in Gastric Cells	9.53	5
5.) Neuroinflammation Signaling Pathway	9.21	9
6.) Role of Macrophages, Fibroblasts and Endothelial Cells in Rheumatoid Arthritis	9.09	9
7.) PI3K Signaling in B Lymphocytes	8.94	7
8.) Neurotrophin/TRK Signaling	8.59	6
9.) Estrogen-Dependent Breast Cancer Signaling	8.5	6
10.) Regulation of IL-2 Expression in Activated and Anergic T Lymphocytes	8.5	6

Table S3. Comprehensive statistical analyses of EP data as shown in Figure 3. Please see associated excel file.

Table S4. Statistical summary data from scRNA sequencing analyses as shown in Figure S8.

Gene	p_val	avg_diff	pct.1 (d93)	pct.2 (d140)	p_val_adj
CEBPD	5.67E-39	-0.2878	0.031	0.1	1.17E-34
NTRK2	1.33E-37	-0.37999	0.11	0.207	2.73E-33
JUNB	1.06E-25	-0.73513	0.18	0.266	2.18E-21
JUN	8.47E-17	0.008603	0.612	0.509	1.74E-12
EGR1	1.26E-11	0.258736	0.579	0.527	2.59E-07
EGR2	1.91E-10	-0.07197	0.077	0.116	3.93E-06
CEBPB	0.000381	-0.01504	0.059	0.042	1
IL17RA	0.023139	-0.01094	0.026	0.035	1
EGR3	0.028882	-0.02342	0.051	0.061	1
IL17RC	0.139015	0.00363	0.024	0.02	1
RELA	0.287542	-0.00825	0.122	0.13	1
FOS	0.296907	-0.33782	0.441	0.456	1

Table S5. Burst detection parameters utilized in Mobius Offline Software.

Burst Detection Parameters	
maximum interval to start burst	300ms
maximum interval to end burst	301ms
minimum number of spikes in a burst*	10 spikes
minimum duration of a burst	50 ms
minimum interval between bursts	200ms
*except for the D34 time point containing 5 minimum number of spikes	
Network Burst Detection Parameters	
minimum percentage of active electrodes	25%
minimum threshold	1,100 spikes/second
bin size	100ms

SUPPLEMENTAL EXPERIMENTAL PROCEDURES

Immunofluorescence analysis. COs, from various designated developmental time points (n=4 from each developmental stage), were transferred to a 4% paraformaldehyde (PFA) solution in PBS and allowed to fix overnight at 4°C. COs were then transferred to a 10% sucrose/PBS solution and allowed to sink before transferring to a 30% sucrose/PBS solution. After COs sank within the 30% sucrose/PBS solution, they were transferred to an embedding tray and immersed in O.C.T (Sakura, Tokyo, Japan). Without introducing air bubbles, COs were then gently moved within the center of the O.C.T solution with a pipette tip. Embedded COs were then rapidly frozen in a dry ice/methanol bath, transferred to a cryostat chuck, and sectioned at 20μm slices using a cryostat (ThermoFisher). Sections were placed onto positively charged glass slides and stored at -20 °C until further immunofluorescence analysis. To perform immunofluorescence analysis, sections were re-hydrated with Tris-buffered saline (TBS), and then incubated in blocking solution containing 0.1% triton X-100 and 10% donkey serum in TBS for 1 hour at RT. Organoid sections were then incubated with primary antibodies at the concentrations designated in Table S1 for 24 hours at 4°C. Sections were then washed with TBS three times for five minutes each before incubation with the secondary Alexa Fluor conjugated antibodies (ThermoFisher) at a 1:500 dilution in blocking solution for two hours at RT. After this incubation, sections were washed with TBS three times for five minutes each and cover-slipped with ProLong Gold Antifade Mountant with DAPI. Primary antibodies and their corresponding descriptions used in this study are shown in Table S1. Confocal microscopy acquisition was performed with a Zeiss LSM confocal fluorescence microscope (models 700 and 800). Fluorescence intensity of GABA and GFAP labeling was performed by acquiring low power images of whole organoid sections from 4 separate COs and then were analyzed using ImageJ software.

Gene expression and pathway analysis. Profiling for genes involved in synaptic plasticity was performed using the RT2 Profile PCR Array human synaptic plasticity kit (Qiagen, Cat # PAHS-126A-2) and the RT2 SYBR Green/ROX PCR Master mix (Qiagen, Cat # 330522) using an ABI Step One plus Real time PCR machine. This gene array

includes primers for 84 transcripts involved in synaptic plasticity, thus allowing for identification of novel gene expression pathways. In brief, total RNA was extracted and purified from the iPS-1 cell line, neuroectodermal bodies, and from the pooling of 5 COs from designated time points using the RNeasy Plus Mini Kit (Qiagen). Three independent qRT-PCR experiments were performed from all samples in this analysis. Data analyses were performed using the GeneGlobe Data Analysis Center Software available on the Qiagen website (https://www.qiagen.com/us/shop/genes-and-pathways/data-analysis-center-overview-page/). Normalization of gene expression was performed using a set of five housekeeping genes and fold regulation was calculated relative to the control iPS-1 cell line. The web tool called Clustvis was used to cluster the row of genes using the Euclidean average clustering method (Metsalu and Vilo, 2015). Fold-change values relative to control hiPSCs were used as input for Clustvis. Genes that were upregulated at three-fold or higher levels within samples relative to control were uploaded into the Ingenuity Pathway Analysis software to identify canonical pathways that involve the upregulated genes, which were then ranked by a statistical scoring algorithm using p-value calculations.

scRNA-seq sample analysis and data processing. Each CO was dissociated into a single cell suspension using a gentleMACS Octo Dissociator (Miltenyi) according to the manufacturer's 37-ABDK02 protocol. In brief, COs were placed in a gentleMACS C Tube (one organoid per C-tube, Miltenyi, 130-093-237) that contained a 2mL solution of Accumax (Sigma, A7089) and then processed on the Octo Dissociator. A 10mL solution of dPBS with 0.04% BSA (Sigma, A9418) was then added to each sample and filtered at 70μm to remove debris. Cell mixtures were then pelleted and resuspended in 1mL dPBS/0.04% BSA. Suspensions were subjected to a second filtration step with a 40μm Flowmi® cell strainer (Sigma, BAH136800040). The concentration and viability of each suspension was determined with a trypan blue stain and hemocytometer.

Raw base call sequencing data were demultiplexed in Illumina’s bcl2fastq and subsequently processed with the 10x Genomics Cell Ranger (v3.1.0) pipeline using data quality that was assessed with the ‘count’ function summary output (D93: 6,172 cells, 23,932 mean reads per cell, 1,762 median genes per cell, 3,988 median UMI counts per

cell; D140: 4,479 cells, 25,435 mean reads per cell, 1,910 median genes per cell, 4,458 median UMI counts per cell) prior to downstream analysis.

Count matrices were loaded into Seurat v3.1.0 (Butler et al., 2018; Stuart et al., 2019) to remove batch effects and apply standard quality control parameters. In brief, cells with <200 and >5,000 unique features or >20% mitochondrial reads were removed from the datasets (4,491 cells from D93 and 4,087 cells from D140 passed). Each organoid's raw UMI count was normalized to its respective total UMI using log-normalization with a scale factor of 10,000 and the top 2,000 variable features per object were identified prior to integration. Integration anchors were identified with 30 principal components and used to combine the two organoid datasets into a single object with a total of 8,578 cells. Then, a linear transformation and dimension reduction analysis (PCA) was applied prior to running a uniform manifold approximate and projection analysis. The dimensionality of this analysis was determined with an elbow plot rank. The FindNeighbors (PCA reduction, 20 dimensions) and FindClusters (0.5 res, 20 dim) Seurat functions were used to carry out KNN unbiased clustering resulting in a total of 13 unbiased clusters. Each cluster's conserved differentially expressed genes were identified with the FindAllMarkers function (Wilcoxon test, min.pct = 0.25, minlogFC = 0.25). These criteria were further refined to only consider a minimum 1.0 log-fold change and two-sided t-test $p<0.05$. The ratio of cells within a given cluster to cells within all other clusters expressing a given marker was also taken into consideration for each defining marker. After evaluating inter- and intra-cluster expression patterns of characteristic canonical markers (Cakir et al., 2019; Quadrato et al., 2017; Velasco et al., 2019) clusters were collapsed into nine categories. Further integrated analyses and visual representations were generated with Seurat and its dependencies.

MEA. Acquisition of spontaneous extracellular field potentials in whole-brain COs was acquired with a 64-channel MEA system (MED64 system, Alpha Med Scientific) at a sampling rate of 20 kHz/channel and at 37°C using a temperature controller device. The MED64 system was connected to a Dell Precision T1700 Tower workstation equipped with an Intel Core i7 4790 (3.6 Ghz) processor. MEA probes (Alpha Med Scientific, Cat # MED-P515A, 64 electrodes, 50µm diameter/100µm spacing) were treated with 0.005%

Polyethyleneimine (PEI) in 25 mM borate buffer (pH 8.4) for ten minutes at RT and then coated with Laminin (Thermofisher, Cat # 23017-015) at a concentration of 2 µg/ml and incubated at 37°C for one hour prior to recording. At D34, we selected 20 COs with similar shape and size that lacked cystic structures to record. We randomly selected 4 of the pre-selected COs at each time point to perform our analyses. To record EP signals, COs (n=4) were transferred from culture to the center of the probe containing the 8x8 channel array using a 1mL pipette with a 1mL tip that was previously cut to a 5mm diameter. Conditioned organoid culture media (approximately ~150 µl) was then placed on the surface of the probe to allow the CO to maintain close proximity with the microelectrodes. Three-minute recordings were performed from all 64 electrode sites, similar to previous studies (Kathuria et al., 2020; Trujillo et al., 2019). Once complete, the COs were placed back into long-term shaking culture conditions. Spikes were detected from raw data using a threshold of 4.25x the SD of the raw signal (Figure 1). Spike data were then imported into MED64 Mobius Offline software (Version 1.4.5) and EP metrics were determined. Electrodes are defined as active by detecting at least 5 spikes/minute (McConnell et al., 2012; Novellino et al., 2011). See Table S5 for burst detection parameters.

REFERENCES

Butler, A., Hoffman, P., Smibert, P., Papalexi, E., and Satija, R. (2018). Integrating single-cell transcriptomic data across different conditions, technologies, and species. Nature biotechnology *36*, 411-420.

Cakir, B., Xiang, Y., Tanaka, Y., Kural, M.H., Parent, M., Kang, Y.J., Chapeton, K., Patterson, B., Yuan, Y., He, C.S.*, et al.* (2019). Engineering of human brain organoids with a functional vascular-like system. Nat Methods *16*, 1169-1175.

Kathuria, A., Lopez-Lengowski, K., Vater, M., McPhie, D., Cohen, B.M., and Karmacharya, R. (2020). Transcriptome analysis and functional characterization of cerebral organoids in bipolar disorder. Genome Med *12*, 34.

McConnell, E.R., McClain, M.A., Ross, J., Lefew, W.R., and Shafer, T.J. (2012). Evaluation of multi-well microelectrode arrays for neurotoxicity screening using a chemical training set. Neurotoxicology *33*, 1048-1057.

Metsalu, T., and Vilo, J. (2015). ClustVis: a web tool for visualizing clustering of multivariate data using Principal Component Analysis and heatmap. Nucleic acids research *43*, W566-570.

Novellino, A., Scelfo, B., Palosaari, T., Price, A., Sobanski, T., Shafer, T.J., Johnstone, A.F., Gross, G.W., Gramowski, A., Schroeder, O.*, et al.* (2011). Development of micro-electrode array based tests for neurotoxicity: assessment of interlaboratory reproducibility with neuroactive chemicals. Frontiers in neuroengineering *4*, 4.

Quadrato, G., Nguyen, T., Macosko, E.Z., Sherwood, J.L., Min Yang, S., Berger, D.R., Maria, N., Scholvin, J., Goldman, M., Kinney, J.P.*, et al.* (2017). Cell diversity and network dynamics in photosensitive human brain organoids. Nature *545*, 48-53.

Stuart, T., Butler, A., Hoffman, P., Hafemeister, C., Papalexi, E., Mauck, W.M., 3rd, Hao, Y., Stoeckius, M., Smibert, P., and Satija, R. (2019). Comprehensive Integration of Single-Cell Data. Cell *177*, 1888-1902.e1821.

Trujillo, C.A., Gao, R., Negraes, P.D., Gu, J., Buchanan, J., Preissl, S., Wang, A., Wu, W., Haddad, G.G., Chaim, I.A.*, et al.* (2019). Complex Oscillatory Waves Emerging from Cortical Organoids Model Early Human Brain Network Development. Cell stem cell *25*, 558-569 e557.

Velasco, S., Kedaigle, A.J., Simmons, S.K., Nash, A., Rocha, M., Quadrato, G., Paulsen, B., Nguyen, L., Adiconis, X., Regev, A.*, et al.* (2019). Individual brain organoids reproducibly form cell diversity of the human cerebral cortex. Nature.